

1 Increasing precipitation due to climate change could partially 2 offset the impact of warming on glacier loss in the monsoon- 3 influenced Himalaya until 2100 CE

4
5 Anya M. Schlich-Davies^{1*}, Ann V. Rowan^{2*}, Andrew N. Ross¹, Duncan J. Quincey³, Vivi K.
6 Pedersen⁴

7
8 ¹Priestley International Centre for Climate, School of Earth and Environment, University of Leeds,
9 UK

10 ²Department of Earth Science, University of Bergen and Bjerknes Centre for Climate Research,
11 Bergen, Norway

12 ³School of Geography, University of Leeds, UK

13 ⁴Department of Geoscience, Aarhus University, Aarhus C, Denmark

14
15 *These authors contributed equally to this work

16
17 Correspondence to: Ann V. Rowan (ann.rowan@uib.no)

18
19
20 **Abstract.** Glacier mass in the Himalaya is projected to shrink by 53–70% due to climate change by
21 2100 CE. However, the impact of changes in precipitation amount and distribution on future glacier
22 change remains uncertain because these variables are not often represented in glacier model projections.
23 We explored the combined effects of past and future changes in air temperature and precipitation
24 amount and distribution on the evolution of Khumbu Glacier in the Everest region of Nepal. We used a
25 glacier modelling approach that forced an ice-dynamical glacier evolution model with surface mass
26 balance calculations that included mesoscale meteorological variables derived from statistical
27 downscaling of existing regional climate projections. Our simulations show that historical warming has
28 committed Khumbu Glacier to mass loss of 10–23% during this century, and that under an intermediate
29 future emissions scenario (RCP4.5), this glacier could lose 70% mass by 2100 CE due to warming. The
30 projected increase in precipitation in tandem with warming could offset about half of the projected
31 glacier loss, such that the total decrease in glacier mass by 2100 CE compared to the present day would
32 be reduced to 34%. However, under a higher future emissions scenario (RCP8.5) glacier loss due to
33 warming will not be compensated by changes in precipitation, but will instead result in substantial
34 ablation above 6,000 m elevation, with devastating consequences for one of the highest glaciers on
35 Earth.

36 37 1. Introduction

38 Projecting glacier change in response to climate change is important for determining the impact of
39 anthropogenic warming on regional water availability (Pritchard, 2019). High Mountain Asia is
40 projected to lose $34 \pm 19\%$ of glacier mass by 2100 CE if warming is limited to 1.5°C to meet the
41 ambitious Paris Agreement target (Kraaijenbrink et al., 2017). Less ambitious projections give $53 \pm$
42 23% glacier mass loss by 2100 CE under the intermediate emissions scenario RCP4.5, and $69 \pm 20\%$
43 under the high emissions scenario RCP8.5 (Kraaijenbrink et al., 2017; Marzeion et al., 2020; Rounce
44 et al., 2023). Such projections are challenging to make, because accumulation and ablation processes
45 in mountain environments are driven by orographic feedbacks between high-relief topography and
46 atmospheric circulation systems such as the South Asian Summer Monsoon (e.g., Bookhagen and
47 Burbank, 2006). Furthermore, large uncertainties arise from the challenge of simulating the interactions
48 between the mass balance regimes of monsoon-influenced glaciers, where accumulation and ablation
49 both occur during the monsoon season, and the dynamics of glaciers flowing through high-relief
50 topography that includes processes such as the development of supraglacial debris layers that modify
51 surface melting (Dehecq et al., 2019; Miles et al., 2018b; Salerno et al., 2023). Variability in the extent
52 and intensity of the Indian Summer Monsoon during the Last Glacial Maximum was shown to affect
53 glacier expansion in the monsoon-influenced Himalaya through changes in snowfall distribution (Benn

54 and Owen, 1998; Owen et al., 2009). Future Indian Summer Monsoon precipitation and variability
55 projected in Global Circulation Models (GCMs) will increase with current global warming
56 (Katzenberger et al., 2021), but as yet, the effect of projected changes in precipitation amount, timing,
57 and phase (rain/snow) on Himalayan glaciers remain poorly constrained (Immerzeel et al., 2012; Mölg
58 et al., 2014; Ragetti et al., 2016; Shaw et al., 2022; Shea et al., 2015).

59
60 Supraglacial debris covers 4–7% of glacier surfaces globally and 30% of glacier ablation areas in the
61 Himalaya, and modifies the response of glaciers to climate change relative to regional trends (Herreid
62 and Pellicciotti, 2020; Kraaijenbrink et al., 2017; Rounce et al., 2023; Rowan et al., 2015). Satellite
63 observations show that the rate of glacier mass loss across the Himalaya has accelerated over the last
64 40 years for both clean-ice glaciers and debris-covered glaciers (Maurer et al., 2019). Observations and
65 modelling studies indicate that thick supraglacial debris caused historical mass loss from debris-covered
66 glaciers to lag that of clean-ice glaciers, such that debris-covered glaciers are currently larger than would
67 otherwise be the case (King et al., 2020; Rounce et al., 2023; Rowan et al., 2021). However, the
68 dampening effect of supraglacial debris on glacier mass loss is overturned by the development of
69 extensive supraglacial ponds and ice cliffs within debris layers (Miles et al., 2018a; Strickland et al.,
70 2023) and the stagnation and detachment of debris-covered tongues from the upper and more active
71 sections of these glaciers (Rowan et al., 2021). Quantifying the impact of feedbacks set up by the
72 formation and expansion of supraglacial debris layers at a regional scale requires exploring such
73 processes at scales that can be resolved in ice-dynamical glacier evolution models (Rowan et al., 2015;
74 Nicholson et al., 2021; Compagno et al., 2022). These processes can be considered in 2-D (along the
75 glacier flowline) either considering stochastic debris delivery to the glacier (Vacco et al., 2010) or
76 continuous debris delivery, which can result in the over-accumulation of debris at the terminus
77 (Anderson and Anderson, 2016; Ferguson and Vieli, 2020; Juvet et al., 2011), or in 3-D (using the
78 horizontal and vertical ice-flow fields), which simulates the lateral transport and deposition of debris to
79 the margins of the ablation area (Rowan et al., 2015; Wirbel et al., 2018). While recent rapid warming
80 has resulted in a rise in regional equilibrium line altitude (ELA) and caused recession and collapse of
81 glacier termini for both clean-ice glaciers and debris-covered glaciers (King et al., 2020), the decay of
82 the former ablation areas of debris-covered glaciers is delayed by supraglacial debris, such that the
83 terminus of the actively flowing glacier can remain in contact with the stagnant former ice tongue rather
84 than separating (Maurer et al., 2019; Pellicciotti et al., 2015; Rowan et al., 2021).

85
86 In common with most large debris-covered Himalayan glaciers, Khumbu Glacier in the Everest region
87 of Nepal (Fig. 1) is in greater imbalance with climate than a climatically equivalent clean-ice glacier,
88 and has maintained a more extensive ice volume than would be possible without supraglacial debris
89 (Rowan et al., 2021). Khumbu Glacier (RGI2000-v7.0-G-15-08331) is 16.0 km long with an area of
90 26.4 km². The median glacier elevation is 6,025 m a.s.l. from the terminus at 4,879 m a.s.l. to the
91 headwall at 7,981 m a.s.l. (RGI 7.0 Consortium, 2023). The stagnant debris-covered tongue has an area
92 of 6.2 km² (23% of the total glacier). As a result of reduced ice flux from the accumulation area, the
93 debris-covered tongue no longer receives much (or any) input of ice, and has dynamically detached
94 from the active glacier (Fig. 1C); this observation is confirmed by the rapid reduction in ice flow and
95 the peak in glacier surface lowering below the Khumbu Icefall where the debris layer is thinnest (King
96 et al., 2020; Quincey et al., 2009). Observations and modelling of the dynamics and structure show that
97 the tongue for 5 km upglacier from the terminus (25% of the total length, 20% of total ice volume) is
98 stagnant and dynamically detached from the active glacier in the last century (Miles et al., 2022;
99 Quincey et al., 2009; Rowan et al., 2021). Basal ice at the glacier surface indicates that the active
100 terminus overrides the stagnant glacier tongue (Miles et al., 2021) and measurements of surface
101 displacement show no longitudinal flow through the detached debris-covered tongue, which is
102 collapsing laterally at a rate of about 3 m a⁻¹ (Watson et al., 2017). Therefore, the active glacier and the
103 stagnant debris-covered tongue evolve along different trajectories, and only the part of Khumbu Glacier
104 above the terminus of the active glacier can be considered dynamic (Miles et al., 2022). Projections of
105 future glacier evolution should therefore discount the heavily debris-covered former tongue, which is
106 decaying *in situ* without any input of new ice from the accumulation area, while considering the
107 development of supraglacial debris across the ablation area of the active glacier.

109 We applied a novel glacier modelling approach to Khumbu Glacier to test the hypothesis that changes
110 in precipitation in response to climate change will reduce the impact of warming on glacier mass loss.
111 Khumbu Glacier is a benchmark debris-covered glacier in the monsoon-influenced Himalaya flowing
112 from 7,981 m above sea level (a.s.l.) to 4,879 m a.s.l. that is representative in terms of elevation of the
113 majority of glaciers in the Central and Eastern Himalaya (Fig. 1B). The ‘Little Ice Age’ (LIA) maximum
114 of Khumbu Glacier occurred about 200–500 years before present, which is consistent with ages
115 produced for moraines elsewhere in the central Himalaya (Hornsey et al., 2022; Rowan, 2017). Khumbu
116 Glacier was slightly larger than today during the late Holocene, transitioning from a clean-ice glacier
117 with high velocities and efficient export of debris to a debris-covered glacier with lower velocities after
118 the LIA; this change was initiated by the reduction in ice flux to the glacier tongue promoted by a rise
119 in ELA (Rowan et al., 2015). We used a 3-D ice-flow model forced by mass balance calculated from
120 mesoscale meteorological variables to simulate the evolution of Khumbu Glacier from the late
121 Holocene (~1 ka) through the present day (2015 CE) until 2100 CE using results from three downscaled
122 Regional Climate Models (RCMs) under two Relative Concentration Pathways (RCPs). This approach
123 represents an advance in the use of such models to understand the evolution of Himalayan glaciers
124 whereby mesoscale meteorological forcing of surface mass balance is used with a thermomechanical
125 glacier model to represent the processes of sublimation, snow avalanching, and debris transport, all of
126 which are important controls on the mass balance of Himalayan glaciers (Kneib et al., 2025).
127 Simulations start from the late Holocene when Khumbu Glacier was last in dynamic equilibrium with
128 the local climate, as evidenced by large ice-marginal moraines dated to 1.3 ± 0.1 ka surrounding the
129 present-day glacier (Hornsey et al., 2022), and when the glacier surface was free of debris (Rowan et
130 al., 2015).

131

132

133 **2. Methods**

134 **2.1 Glacier model experimental design**

135 The glacier model experiments used mesoscale meteorological variables to calculate surface mass
136 balance for the Khumbu Glacier catchment in combination with a debris-covered glacier evolution
137 model to represent the surface processes that modify mass balance (Fig. 2A). Our approach produced a
138 total of six simulations of Khumbu Glacier to 2100 CE from three CORDEX South Asia region RCMs
139 (NOAA, CCCma, IPSL; Lutz et al., 2016) under two RCPs (RCP4.5 and RCP8.5; Collins et al., 2013)
140 to explore the impacts of possible variability in future precipitation amount and distribution in tandem
141 with warming on glacier evolution. Before we used the RCMs to force the future climate scenarios, we
142 evaluated their capabilities against observations of present-day weather and climate. The experimental
143 design represents an advance compared with previous glacier modelling efforts by including in each
144 simulation; (1) mesoscale meteorological phenomena, including sublimation, (2) the redistribution of
145 surface mass by snow avalanching, and (3) the feedbacks between debris transport, ice flow and mass
146 balance. This section describes the experimental design for the glacier modelling workflow,
147 downscaling of the present-day RCMs using meteorological data from automatic weather stations
148 (AWS) in the Khumbu Valley, downscaling of the future RCMs for both RCPs, the surface energy and
149 mass balance calculations using COSIPY (Sauter et al., 2020) and the debris-covered glacier evolution
150 modelling using iSOSIA (Rowan et al., 2015). A reference simulation and sensitivity experiments were
151 carried out for the period 2013–2015 CE, and the simulations of future glacier change represented the
152 period 2015–2100 CE. Additional information about the development and testing of the modelling
153 approach is provided in Appendix A.

154

155 The spin-up simulation from the ice-free model domain to represent the late Holocene glacier was
156 forced using a simple approximation of mass balance. The ice-free model domain was found by
157 subtracting the estimated ice thickness (Farinotti et al., 2019) from a 30-m digital elevation model
158 (DEM) acquired from the Shuttle Radar Topography Mission (Farr et al., 2007). The ice-free model
159 domain incorporated the full hydrological catchment including the steep hillslopes in the Western Cwm
160 that provide snow to the glacier surface by avalanching. As a starting point for our transient simulations
161 of Khumbu Glacier, we reconstructed the late Holocene glacier from the ice-free domain using an ELA
162 of 5,325 m a.s.l. and an atmospheric lapse rate of $-4.0^{\circ}\text{C km}^{-1}$ in a 5,000 year simulation. Accumulation
163 above the ELA was calculated as a function of elevation 0.2 m m^{-1} up to a maximum of $2.0 \text{ m w.e. a}^{-1}$

164 and ablation was calculated as a function of elevation 0.5 m m^{-1} up to a maximum of $2.0 \text{ m w.e. a}^{-1}$.
165 This simulation continued through the LIA forced by a step change in mean annual air temperature
166 (MAAT) equivalent to 1.5°C colder than the present day over 500 years following the approach of
167 Rowan et al. (2015, 2021). Ice-marginal moraines denoting the late Holocene ($1.3 \pm 0.1 \text{ ka}$) glacier
168 extent and thickness (Hornsey et al., 2022) were used to constrain the spin-up simulation.
169

170 The late Holocene simulation was forced to present-day (2015 CE) conditions using three surface mass
171 balances (one from each RCM) calculated using the Coupled Snowpack and Ice-surface Energy and
172 Mass Balance model in Python (COSIPY v1.3) (Sauter et al., 2020). These simulations were evaluated
173 against a range of observations of present-day glaciology and previous glacier model experiments (Fig.
174 3), and the experiment using the NOAA RCM was identified as the starting point for all future
175 simulations because this was most representative of the observed glacier. We simulated only the active
176 section of the glacier beyond 2015 CE and added the dynamically detached debris-covered tongue
177 simulated at the present day to the model domain as a static topographic feature for the future
178 simulations. The volume of the detached tongue was calculated by using the simulated present-day
179 velocity field to separate the simulated present-day ice volume where velocities declined below 10 m
180 a^{-1} . Thus, we arrived at the present-day from the LIA maximum simulation by forcing the LIA glacier
181 with the 2015–2020 CE mass balance.
182

183 We used the output from the present-day simulation with the 2095–2100 CE mass balance calculated
184 using COSIPY to force the model to 2100 CE. The glacier model simulations continued from the present
185 day to 2100 CE forced by distributed glacier surface mass balances calculated for each of the three
186 RCMs and two RCPs using COSIPY. The three RCMs and two future RCPs represented a range of
187 possible future climates with distinctly different precipitation trends—equivalent to dry, moderate, and
188 wet scenarios for warming of $1.4\text{--}2.2^\circ\text{C}$ under RCP4.5 and $3.8\text{--}4.1^\circ\text{C}$ under RCP8.5 (Table 1; Fig. 2D;
189 Section 2.3). We used time slices representing the present day (2015–2020 CE) and the end of the 21st
190 Century (2095–2100 CE) to calculate surface mass balance, and the preceding decade was used to
191 evaluate these time slices (see Section 3.3). We used this step forcing, whereby the future mass balance
192 was imposed and the glacier adjusted to this from the start of the century in question, rather than
193 interpolating mass balance over time to reduce the computational expense of the surface mass balance
194 and glacier modelling (~24 hours per simulation).
195

196 Estimates from a global glacier modelling study indicate that avalanching contributes up to 18% of
197 regional accumulation to glaciers in the monsoon-influenced Himalaya (Kneib et al., 2025) and
198 observations of high-elevation Himalayan glaciers, including Khumbu Glacier, suggest that up to 75%
199 of accumulation occurs by avalanching rather than direct snowfall (Fig. 1D) (Benn and Lehmkuhl,
200 2000; Laha et al., 2017). Avalanching affects mountain glaciers in two ways; (1) by moving snow from
201 steep hillslopes onto the glacier surface thus increasing accumulation from that calculated from direct
202 snowfall onto the glacier surface, and (2) by redistributing snow across steep sections of the glacier
203 surface (Kneib et al., 2025). We examined the uncertainty in accumulation resulting from the application
204 of a calculation in iSOSIA to move snowfall from slopes susceptible to avalanching (see Section 2.6).
205 If avalanching was not considered in iSOSIA, then the accumulation of snow calculated using COSIPY
206 within the catchment but outside of the glacier outline would have no impact on accumulation resulting
207 in an underestimation of ice volume, and the steep sections of the glacier would hold more mass than
208 expected. For example, when avalanching was not simulated and accumulation occurred at a uniform
209 rate of $2.0 \text{ w.e. m a}^{-1}$ across the Western Cwm accumulation area, Khumbu Glacier had a similar extent
210 but a volume more than double that of the glacier simulated with avalanche redistribution of snow,
211 because mass was not redistributed effectively across steep sections of the glacier surface (result not
212 shown).
213

214 **2.2 Meteorological data collection and analysis**

215 The first meteorological observations for the Nepal Himalaya were collected during the 1970s and
216 found a trend of diurnal precipitation on ridges and nocturnal precipitation in valley floors (Ageta, 1976)
217 reflecting cloud development from orographic convection during the day. Continuously recording AWS
218 were first installed in the region in the 1990s at the Pyramid Observatory near Lobuche village, where

219 Bollasina et al. (2002) analysed of the monsoon from meteorological observations collected between
220 1994 and 1999, finding that the onset (decay) of the Indian Summer Monsoon was distinguished by
221 higher (lower) daily precipitation totals, mean relative humidity and atmospheric pressure and a reduced
222 (increased) diurnal range in atmospheric temperature. Bollasina et al. (2002) identified two daily
223 profiles in precipitation and wind direction thought to be related to the monsoon. In addition, five-day
224 and ten-day precipitation cycles were observed linked to oscillations in the Tibetan High. A new AWS
225 was installed at the Pyramid Observatory at 5,035 m a.s.l. in September 2000 as part of a network in
226 the Dudh Koshi valley of six AWS between 2,680 to 5,700 m a.s.l., in addition to some short-lived
227 higher-elevation stations, maintained by the Ev-K2-CNR network. The Pyramid Observatory AWS
228 included a snow depth sensor between 2009 and 2010, but the data were discontinuous and inconsistent,
229 and the measurement period ended in December 2010. A second AWS was installed in the same location
230 by the GlacioClim network in 2013 (Wagnon et al., 2013; Sherpa et al., 2017) provides a longer period
231 of continuous data collection. More recently, a network of 5 AWS including the highest elevations in
232 the Khumbu catchment were installed by the National Geographic project at Phortse (3,810 m a.s.l.),
233 Everest Base Camp (5,315 m a.s.l.), Camp 2 (6,464 m a.s.l.), the South Col (7,945 m a.s.l.) and the
234 Balcony (8,430 m a.s.l.) (Matthews et al., 2020). However, at time of writing, there are no continuous
235 records of high-elevation meteorological variables that span a longer period than 15 years, making the
236 calculation of climate normals impossible. In this study, we analysed data from these various sources
237 for evaluation of mesoscale trends in the upper Khumbu Valley and for use to downscale RCMs and
238 evaluate the results of our calculations. The location of the AWS is shown in Fig. 1C. Gaps in the air
239 temperature and precipitation data were filled using interpolated data from neighbouring stations where
240 required (as described in Appendix A).

241
242 The AWS data were used to make a reference simulation in COSIPY of the surface energy fluxes and
243 mass balance of the Khumbu Glacier catchment between 2013–2015 for model development and
244 sensitivity experiments (Fig. 4 and Fig. 5). We compiled 14 years of meteorological observations from
245 the two AWS provided by the GlacioClim network at the Pyramid Observatory (5,050 m a.s.l. and 5,035
246 m a.s.l.) and the West Changri Nup Glacier AWS (5,363 m a.s.l.) (Wagnon et al., 2013; Sherpa et al.,
247 2017). All meteorological data were collected for the period December 2010 to November 2019, apart
248 from precipitation which was only recorded between December 2012 to November 2016. All
249 meteorological data (excluding precipitation) used for the reference simulation were taken from the
250 West Changri Nup AWS. Given the frequency of missing precipitation data from the AWS, the
251 undercatch of snow associated with tipping bucket rain gauges, and the scarcity of high-elevation
252 precipitation measurements, precipitation was not varied with elevation in the reference simulation.
253 Precipitation data for the reference simulation were collected from the GlacioClim Geonor precipitation
254 gauge at the Pyramid Observatory (5,035 m a.s.l.) because this precipitation gauge provides a longer
255 period of continuous observations than the other gauges and avoids errors due to low precipitation
256 amounts measured by tipping bucket gauges, which are known to systematically underestimate snowfall
257 particularly during high winds (Sherpa et al., 2017). Precipitation was measured at 15-minute intervals
258 using a Geonor T-200BM sensor mounted 1.8 m above the surface. Evaporation from the bucket was
259 blocked by a layer of oil, but some loss did occur, as evidenced by precipitation values below 0 mm.
260 Noise from wind and evaporation were corrected for by compensating any negative change over the
261 15-minute time step with the neighbouring positive value such that accumulated precipitation was
262 unchanged. Periods with prolonged evaporation were set to zero. Undercatch of snowfall by rainfall
263 gauges was corrected through precipitation phase partitioning using wind speed observations (Wagnon
264 et al., 2009). Air temperature was interpolated to match the height of the precipitation gauge using
265 hourly lapse rates that averaged $-5.89\text{ }^{\circ}\text{C km}^{-1}$. COSIPY was run for both elevations using the non-
266 adjusted temperature data for 5,336 m a.s.l. and the adjusted temperature data for 5,035 m a.s.l. and it
267 made little impact on the model results. Simulated meteorological variables were evaluated at the
268 highest elevations using the National Geographic AWS stations at Camp 2 (6,464 m a.s.l.) and the South
269 Col (7,945 m a.s.l.) using data for May–November 2019 (Matthews et al., 2020).

270
271 Direct solar radiation across the model domain was corrected for the slope, azimuth, and shadowing
272 potential of each pixel (Wohlfahrt et al., 2016; Sauter et al., 2020). A footprint-weighted correction was
273 also applied to horizontal measurements of net radiation. The fraction of diffuse incoming shortwave

274 radiation was estimated by using the ratio of total shortwave (global) radiation and potential shortwave
275 radiation to define a clearness index (Wohlfahrt et al., 2016). This clearness index was used to calculate
276 diffuse radiation, which was calibrated with data from the Neustift eddy covariance station in the
277 Austrian Alps (Wohlfahrt et al., 2008). Pressure was distributed across the domain by first calculating
278 sea-level pressure (*cf.* Lente and Osz, 2020) and then interpolated with the barometric equation. The
279 relative humidity gradient was calculated as -0.002 \% m^{-1} using data from the Ev-K2-CNR and the
280 GlacioClim AWS networks, and evaluated by comparison with measurements made by the National
281 Geographic network AWS ranging in elevation from 3,810–8,430 m a.s.l. (Matthews et al., 2020) to
282 capture trends at higher elevations. The distributed radiative fluxes were compared with the same high-
283 elevation stations for 2019 to assess the efficacy of this method across the domain. Wind speed was
284 assumed to be uniform across the domain.

285

286 **2.3 Present-day RCM downscaling using meteorological observations**

287 Six RCMs were assessed on their fidelity to present-day climate using hindcasting (Biemans et al.,
288 2013) with an emphasis on temperature seasonality and seasonal precipitation dynamics given the
289 importance of these variables for glacier mass balance. RCMs from the Coordinated Regional
290 Downscaling Experiment (CORDEX) South Asia domain were dynamically downscaled from CMIP5
291 GCMs by the Indian Institute of Tropical Meteorology to a 50 km spatial resolution (Lutz et al., 2016)
292 and collected for the grid box containing Khumbu Glacier (27.9065056°N, 86.4352951°E). Three of
293 the six CORDEX South Asia RCMs (NOAA, CCCma, IPSL) spanning a range of possible future
294 precipitation conditions (Table 1) were selected as discrete scenarios for the glacier surface energy and
295 mass balance calculations. The three remaining RCMs were discounted due to being intermediate to
296 those selected for our experiments (*i.e.* close to the future precipitation scenario represented by CCCma)
297 or particularly poor at reproducing seasonal temperature and precipitation cycles. For example, despite
298 the annual precipitation sums from the CSIRO RCM being closest to observed values and having the
299 potential to be the ‘driest’ scenario examined, analysis of precipitation seasonality indicated that the
300 monsoon signal was completely absent with this RCM instead showing a strong dominance of winter
301 precipitation.

302

303 The present-day RCM results were downscaled using quantile mapping, also known as “distribution
304 mapping”, using 14 years of observations collected between January 2006 and November 2019 from
305 three AWS as described in Section 2.2. Parametric quantile mapping (Piani et al., 2010) was used to
306 downscale the RCM to a daily time step at the resolution of the DEM, whereby a statistical relationship
307 between the raw climate model outputs and observations was formed by substituting the RCM results
308 with observations at a cumulative density function of the prescribed distribution (*e.g.*, a Gaussian
309 distribution for temperature; Luo et al., 2018; a gamma distribution for precipitation; Piani et al., 2010).
310 This correction was applied to the raw RCM outputs to produce a third downscaled dataset which had
311 an improved the fit to the observations (Fig. 2C and 2D). The quantile mapping approach was chosen
312 because this is effective for downscaling precipitation and reduces errors in the standard deviation, the
313 coefficient of variation, and the skewness of distributed values relative to other methods (Lafon et al.,
314 2013; Reiter et al., 2018). The AWS data were used to disaggregate the daily downscaled present-day
315 and end-of-century climate model outputs to an hourly resolution for energy balance modelling. All
316 meteorological variables, excluding precipitation, were downscaled using the MELODIST Python tool
317 (Förster et al., 2016). Seasonal means were applied for precipitation to reproduce the ‘nocturnal peak’
318 seen during the monsoon that MELODIST was unable to replicate (Figs. A1, A2 and A3). Further
319 information on the meteorological data analysis and RCM downscaling are provided in Appendix A.

320

321 **2.4 Future RCM downscaling**

322 Two future emission scenarios (RCP4.5 and RCP8.5) were available from CORDEX South Asia, which
323 represent intermediate and high emissions by 2100 CE relative to the present day. These two emissions
324 scenarios are frequently used in climate impact studies enabling the comparison of our results with
325 studies that use other climate/glacier model projections. The two future emissions scenarios were
326 analysed for each of the three CORDEX RCMs to account for the inherently high uncertainties in future
327 precipitation trends associated with climate models and the interplay of changing precipitation with
328 atmospheric warming. The same statistical downscaling approach and disaggregation used for the three

329 present-day RCMs described in Section 2.3 was applied to the raw CORDEX RCM daily outputs for
 330 the three future RCM time slices under RCP4.5 and RCP8.5. The temperature change between the
 331 present day and the future time slices was preserved and there was no evidence of any imposed
 332 strengthening in the monsoon resulting from downscaling. An increase in the frequency of days per
 333 year outside of the monsoon season with high precipitation amounts (defined here as over 15 mm of
 334 daily precipitation) accounted in large part for the higher annual precipitation amounts relative to the
 335 present day that were found in four out of the six RCMs. However, the total future annual precipitation
 336 increase was on average 8.8% greater in the downscaled climates relative to the raw RCMs, suggesting
 337 that this positive trend was inflated by downscaling. The downscaled climates reduced the frequency
 338 of precipitation, although, as in present day observations, monsoon precipitation occurred frequently
 339 and could be characterised as predominantly drizzle in the future.

341 2.5 Surface energy balance modelling

342 COSIPY is a leading open-source method for estimating glacier surface mass balance and has
 343 previously been applied to glaciers in High Mountain Asia. COSIPY includes a calculation of
 344 sublimation, which is an important ablation process for high-elevation glaciers because ablation can
 345 still occur if the latent heat flux is negative through sublimation, even in instances where surface
 346 temperature and/or air temperature are well below the melting point (Bonekamp et al., 2021; Brun et
 347 al., 2023; Huintjes et al., 2015). COSIPY resolves all energy fluxes (F) at the ice surface that contribute
 348 to surface melt (Q_{melt}):

$$349 \quad F = SW_{in} \cdot (1-\alpha) + LW_{in} + LW_{out} + Q_{sens} + Q_{lat} + Q_g + Q_{liq} \quad \text{Eq. (1)}$$

350
 351
 352 Where SW_{in} is incoming shortwave radiation, α is albedo, LW_{in} and LW_{out} are incoming and outgoing
 353 longwave radiation, and Q_{sens} , Q_{lat} , and Q_g are the sensible, latent, and ground heat fluxes (Oerlemans
 354 et al., 2001) and Q_{liq} is the heat flux from liquid precipitation; the latter variable is often neglected in
 355 ablation calculations (Cuffey and Paterson, 2010) but is of particular importance here as the Indian
 356 Summer Monsoon brings a significant amount of liquid precipitation to the lower reaches of Khumbu
 357 Glacier. The resulting F is equal to the energy available for surface melt (Q_{melt}) when surface
 358 temperature (T_s) is at melting point (0°C). T_s is used to calculate LW_{out} , Q_{sens} , Q_{lat} , Q_g and to partition
 359 solid and liquid precipitation. When T_s exceeds the melting point it is reset to 0°C (273.15 K) and the
 360 residual F fluxes equal Q_{melt} . In this instance, subsurface melt is triggered when the energy fluxes, for
 361 example, penetrating SW_{in} warm the ice layer so that T_s exceeds the melting point of ice (Sauter et al.,
 362 2020).

363
 364 The COSIPY model domain was taken from the 30-m DEM that was resampled to 200-m grid spacing
 365 following a reference simulation for 2013–2015 and sensitivity analyses, which revealed minimal
 366 impact on the results whilst greatly reducing computational expense (Fig. 4). The sensitivity of glacier
 367 mass balance to individual meteorological variables (MAAT, radiative fluxes, relative humidity, lapse
 368 rate, precipitation amount, precipitation phase, glacier surface roughness) was calculated in sensitivity
 369 experiments using the reference simulation that perturbed these variables individually. Perturbations
 370 were made within the range of the possible uncertainties for each variable that arise from a combination
 371 of the choice of observations or climate models, the downscaling approach used, and the distribution of
 372 meteorological variables (see Section 3.1). The values used for perturbations of MAAT and
 373 precipitation amount were similar to those expected for possible future climate forcings. We tested a
 374 range of lapse rates from $-3.0^\circ\text{C km}^{-1}$ to $-6.0^\circ\text{C km}^{-1}$ while maintaining the same ELA based on the
 375 range of monthly values calculated from regression of NASA MODIS land surface temperature data for
 376 the Central Himalaya, which resulted in a difference in ice volume of $0.4 \times 10^9 \text{ m}^3$ and no change in
 377 glacier length at the present day (result not shown).

378
 379 The downscaled and disaggregated CORDEX RCM daily climate variables (temperature, precipitation,
 380 the radiation components, wind speed, relative humidity and atmospheric pressure) were used to force
 381 COSIPY for the periods 2015–2020 CE and 2095–2100 CE. While snowfall measurements can be used
 382 as an input to COSIPY, there are no good-quality measurements of snowfall in the Everest region and
 383 so precipitation was partitioned into rainfall and snowfall using the snow transfer scheme within

384 COSIPY (Sauter et al., 2020). COSIPY was forced using hourly meteorology with nine variables to
 385 calculate the energy balance and mass balance components at an hourly time step from the sum of
 386 accumulation by solid precipitation, deposition, and refreezing of melt water percolation, and ablation
 387 by melt and sublimation. The exchange processes at the surface, including energy release and
 388 consumption with phase changes, control temperature distribution and phase changes within the glacier
 389 (comprised of horizontal ice and snow layers), and accounts for meltwater refreeze and percolation with
 390 the meltwater produced from the surface melt calculations acting as an input. The impacts of
 391 supraglacial debris on ablation and of snow avalanching on accumulation were handled in iSOSIA, as
 392 described in the next section.

393 2.6 Ice-dynamical glacier evolution modelling

394 The second-order shallow ice approximation model (iSOSIA) is a 3-D higher-order ice-dynamical
 395 glacier evolution model that solves for the flow of ice including longitudinal and transverse stress
 396 gradients that are imposed on ice flow through high-relief topography (Egholm et al., 2011). This glacier
 397 model simulates the evolution of debris-covered glaciers by incorporating the feedbacks between debris
 398 transport, mass balance and ice flow (Rowan et al., 2015) and includes two processes that are important
 399 for many Himalayan glaciers; (1) the redistribution of snow by avalanching that is estimated to account
 400 for up to 75% of accumulation, and (2) the formation and evolution of a supraglacial debris layer that
 401 insulates the ice surface to modify ablation (Rowan et al., 2015). While previous versions of this glacier
 402 model used depth-integrated ice flow, this version simulates ice flow through Khumbu Glacier in 3-D
 403 as the ice thickness is divided into 20 vertical layers to calculate englacial debris transport (Rowan et
 404 al., 2015). The glacier model has a variable time step that can adjust up to a maximum of 0.1 years to
 405 allow greater computational efficiency.

406 The distributed surface mass balances calculated using COSIPY using the downscaled RCMs for the
 407 periods 2015–2020 CE and 2095–2100 CE were used as inputs to the glacier model with no change in
 408 forcing applied between these two periods. The model domain topography was the same in iSOSIA as
 409 that used in COSIPY. Surface processes within the glacier model modified the distribution of
 410 accumulation and ablation but this was not updated into the surface topography used in COSIPY.
 411 Simulated accumulation was the result of the total snowfall in each cell and avalanching of snow
 412 imposed for the accumulated snowpack from hillslopes by removing snow and ice from hillslopes
 413 greater than 28° and redistributing this mass across less steep surfaces using a non-linear hillslope flux
 414 model (Roering et al., 1999). The avalanching routine was found to be sufficient to prevent snow and
 415 ice accumulation on slopes that are observed to be free of glacier ice such as the southwest face of
 416 Sagarmatha (Mt. Everest) while allowing accumulation on steep sections of the glacier (Rowan et al.,
 417 2015) resulting in accumulation rates at the glacier surface in line with the limited available
 418 observations for Himalayan glaciers of 2 m water equivalent (w.e.) per year (Benn and Lehmkuhl,
 419 2000).

420 Rock avalanching is responsible for much of the debris accumulation on the glacier surface but there is
 421 little information about the magnitude and frequency of these events, so headwall erosion was assumed
 422 to be uniform at 1 mm a⁻¹ (Rowan et al., 2021). Debris produced by headwall erosion was delivered to
 423 the glacier surface using a similar non-linear hillslope flux model to snow avalanching. The reduction
 424 in ablation beneath supraglacial debris from clean-ice values was represented as a reciprocal function
 425 that scaled clean-ice ablation (b_{clean}) to give sub-debris melt (b_{debris}) as a function of debris thickness
 426 (h):

$$427 \quad b_{debris} = b_{clean} \times \frac{h_0}{h + h_0} \quad \text{Eq. (2)}$$

428 where h_0 is a constant representing the characteristic debris thickness at which the reduction in ablation
 429 due to insulation by supraglacial debris is 50% of the value for an equivalent clean-ice surface
 430 (Anderson and Anderson, 2016; Rowan et al., 2021). The observed heterogeneity of surface ablation
 431 required a parameterisation of sub-debris melt representing the effects of differential ablation, which
 432 was represented in Equation (2) using a value for h_0 of 0.8 m (Bartlett et al., 2021; Rowan et al., 2021;

438 Strickland et al., 2023). We note that Equation (2) represents an empirical calculation of the impact of
439 supraglacial debris on glacier surface melt that is calibrated to observations of sub-debris melt rates for
440 glaciers in the Central Himalaya (Rowan et al., 2021) and as such, changes in surface energy balance
441 processes including vapour fluxes within the debris-covered section of the glacier are not included.

442

443 3. Results

444 3.1 COSIPY parameter perturbations

445 The spatially averaged mass balance was most sensitive to changes in MAAT (perturbed by $\pm 1.5^\circ\text{C}$,
446 2.0°C and 3.0°C), $LWin$ and $SWin$ ($\pm 10\%$ and 20%). Perturbations of relative humidity ($\pm 10\%$ and
447 $\pm 20\%$) had the least impact on mass balance. The use of a seasonal lapse rate of $5.38^\circ\text{C km}^{-1}$ yielded a
448 spatially averaged mass balance that was 5.6% less than the reference calculation value, while a diurnal
449 lapse rate gave a mass balance that was only 0.45% lower because the reference lapse rate was close to
450 the mean of the day/night lapse rates, whereas the environmental lapse rate ($6.50^\circ\text{C km}^{-1}$) gave a mass
451 balance that was 1.24% higher than the reference value. The relatively small difference in mass balance
452 due to the choice of lapse rate is due to the extremely high elevation of Khumbu Glacier, which means
453 that MAAT is below 0°C in the accumulation area for much of the year and a higher lapse rate does not
454 affect rain/snow partitioning. The largest difference in mass balance due to the choice of lapse rate
455 occurred just below the ELA and resulted in a difference of $\pm 24\%$ in spatially averaged mass balance
456 for this section of the glacier. The National Geographic AWS on Mt. Everest provided an opportunity
457 to examine lapse rates at the highest elevations. For the period April–November 2019, the observed
458 lapse rate was $4.68^\circ\text{C km}^{-1}$ between Phortse (3,810 m a.s.l.) and Everest Base Camp (5,315 m a.s.l.),
459 and $5.36^\circ\text{C km}^{-1}$ between Camp II and South Col, similar to the value used in this study. The lapse rate
460 above 8,000 m a.s.l. was about $1.2^\circ\text{C km}^{-1}$ greater than that below 5,600 m a.s.l. between the two highest
461 AWS at the South Col (7,945 m a.s.l.) and the Balcony (8,430 m a.s.l.) indicating that in the highest-
462 elevation sections of the catchment, lapse rates may be best represented by values considered suitable
463 for the free atmosphere.

464

465 Coupled parameter testing was carried out to perturb precipitation and MAAT simultaneously. The most
466 significant change in spatially averaged mass balance followed a 3°C increase in MAAT and 20%
467 decrease in precipitation amount. The change in ablation following an increase in temperature of 1.5°C
468 was compensated by accumulation resulting from 20% higher precipitation. The impact on mass
469 balance of two precipitation phase (rain/snow) partitioning schemes was investigated and compared
470 with the default snow transfer function in COSIPY; (1) using threshold temperatures of 0.5°C , 2.0°C ,
471 and 3.5°C , and (2) using a calculation that smoothly scaled rain/snow partitioning from 100% solid
472 precipitation at -1°C to 0% solid precipitation at 4°C . The height of the 0°C isotherm during months
473 that experienced significant ablation (May–September) fluctuated around 5,125–6,250 m a.s.l., which
474 correlated with the elevations that experienced the greatest mass balance change with lapse rate. While
475 the lapse rate used to distribute MAAT did not have a significant impact on glacier-wide mass balance,
476 the elevation of the 0°C isotherm from the pre-monsoon until the end of the monsoon was sensitive to
477 the air temperature distribution.

478

479 The glacier ice surface roughness (z_0) value was 1.7 mm (Table 2), which is a reasonable estimate for
480 clean-ice glaciers (Mölg et al., 2012). The z_0 values reported in the literature vary widely, even for clean-
481 ice glaciers, and do not consider debris-covered glacier surfaces, and so two substantially different z_0
482 values were tested as end-members of the likely range in z_0 values for Khumbu Glacier. Values for z_0 of
483 0.1 mm from Midtre Lovénbreen in Svalbard (Irvine-Fynn et al., 2014) and August-One Glacier in
484 China (Guo et al., 2018), and a value of 6.9 mm for the clean-ice section of Haut Glacier D’Arolla
485 (Brock et al., 2006) were all tested in the reference simulation. Adjusting z_0 had minimal impact on
486 mass balance, although a higher (lower) z_0 did result in slightly increased (decreased) mass balance.

487

488

489 3.2 Evaluation of the COSIPY surface energy balance model results

490 The reference simulation represented the period 2013–2015 CE and was forced with AWS data using
491 the model parameters in Table 2. Turbulent fluxes and energy balance components across Khumbu
492 Glacier were explored across the 2013–2015 reference period to assess the performance of COSIPY

493 and understand their relative spatial importance (Fig. 5). The glacier-wide clean-ice mass balance for
494 the three-year reference period was -3.4 m w.e, which equates to -1.13 m w.e a^{-1} . Maximum ablation
495 was up to 16.2 m w.e. over three years (Fig. 4). High precipitation events were observed to offset some
496 ablation if they occurred outside the core monsoon season (e.g., in October 2013 and May 2014) but
497 did not influence monsoon season ablation when high air temperatures and strong incoming radiative
498 fluxes rapidly remove snow cover and drive melting. Higher minimum temperatures in winter 2013–
499 2014 CE relative to the other winters did not significantly influence accumulation rates, which remained
500 similar to those in 2014–2015 CE. Low precipitation amounts during the 2015 monsoon (286 mm in
501 2015, compared to 330.8 mm in 2013, and 333.9 mm in 2014) resulted in lower accumulation in the
502 upper reaches of the glacier. The precipitation gradient was calibrated to $1 \times 10^{-5} \% m^{-1}$ to match
503 observed accumulation rates. However, this gradient largely arises from avalanching (Benn and
504 Lehmkuhl, 2000) which is challenging to represent in COSIPY and was instead handled in the glacier
505 model (Section 2.6).

506
507 The energy available for ablation peaked in the pre-monsoon and monsoon, bringing higher rates of
508 sublimation and subsurface melt in April–June (Fig. 5). Simulated sublimation occurred at all
509 elevations, with the highest cumulative loss near the South Col (EB7910) where sublimation dominated
510 mass balance and only slightly slowed from December until May. Sublimation rates were increasingly
511 tied to seasonality with distance down-glacier, with rates on the lower section of the tongue (EB4980)
512 increasing from April until the start of the monsoon in July. Calculated subsurface melt was negligible
513 at or above the ELA ($5,950$ m a.s.l.) whereas at lower elevations sub-surface melt dominated mass
514 balance with a stronger seasonal cycle related to surface temperature. The interannual variability in
515 subsurface melt was linked to surface temperature, although low simulated subsurface melt rates in the
516 first year of the reference simulation were largely due to persistence of the initial snow cover that
517 shielded the subsurface from relatively warm air temperatures until the subsurface adapted to local
518 conditions. Refreezing occurred across the entire glacier, with a staggered onset due to increased
519 elevation, and the absolute values were low (Fig. 5). The higher latent heat flux during the monsoon
520 resulted in higher deposition of snow to the glacier at the lower elevations, with negligible rates at
521 higher elevation. Similar absolute values and patterns are seen for condensation.

522
523 Calculated incoming shortwave radiation matched well with AWS observations, indicating that the
524 radiation model in COSIPY performed well across the extreme relief of the Khumbu Glacier catchment.
525 Net shortwave radiation contributed the largest energy input to the glacier surface at lower elevations,
526 correlating most strongly with the energy available for melt, with a mean correlation coefficient of 0.79 .
527 There was high temporal variability related to variable cloud cover exhibited in the hourly incoming
528 shortwave radiation forcing and fluctuating albedo during the warmer months with the melting of the
529 snowpack. The high incoming shortwave radiation the upper reaches of the glacier indicate that low net
530 shortwave radiation is not due to topographic shading. Net shortwave radiation was correlated with
531 albedo ($r = 0.86$), and the persistence of snow throughout much of the year reduced the energy available
532 for melt. Net longwave radiation also contributed to the energy available for melt as the pattern of both
533 fluxes corresponded. Between $5,900$ – $7,900$ m a.s.l., net longwave radiation sometimes exceeded zero
534 during the monsoon, most likely due to heavy cloud cover and increased temperatures relative to the
535 glacier surface. The latent heat flux was almost zero at the lower elevation sites as the arrival of the
536 monsoon resulted in higher relative humidity, and this pattern was similar, but dampened, at higher
537 elevation. At the South Col (EB7910) the energy available for melt correlated most closely with the
538 sensible heat flux (Fig. 5).

539
540 Grid spacings for the model domain of 30 m, 50 m, 200 m and 1 km were tested to ensure that that the
541 COSIPY calculations captured orographic effects without unnecessary computational expense (Fig. 4).
542 The simulated maximum accumulation rate did not change significantly with grid spacing, giving
543 accumulation rates of 2.1 – 3.9 m w.e. at $6,500$ – $7,000$ m a.s.l. in the reference simulation. The 1 km grid
544 spacing contained only 27 glacier points, and gave a similar spatial mean mass balance to the finer-
545 resolution calculations, but there were large gaps in mass balance calculated across the glacier that
546 affected the height of the ELA and significantly reduced the calculated maximum accumulation value.
547 The 30 -m and 50 -m grid spacings captured greater spatial variability in mass balance relative to the 200

548 m resolution calculation, particularly at elevations between 5200–5400 m a.s.l. (Fig. 4). However, as
549 the ELA, and the calculated maximum and minimum mass balances were not significantly different
550 between these finer-resolution calculations, the 200 m grid spacing was used throughout to benefit from
551 the much reduced computational expense.

552

553 **3.3 Evaluation of the RCM downscaling**

554 The downscaled climate variables from the three RCMs for the present-day time slices (2015–2020 CE)
555 were evaluated against 14 years of observations from three AWS to assess the representation of means,
556 seasonality, diurnal cycles, day-to-day variability, and interannual variability (Fig. 2C and 2D). All three
557 downscaled RCMs showed good agreement between MAAT ($-2.15 \pm 0.05^\circ\text{C}$) and observed air
558 temperature from the Pyramid AWS (Figs. A1 and A2). The representation of the monsoon was greatly
559 improved by the RCM downscaling; temperature seasonality was well resolved following quantile
560 mapping and the monthly mean and minimum air temperatures were similar to observations across the
561 present-day time slice (Fig. A1). The monsoon stabilised air temperatures and reduced the range
562 between minimum and maximum temperatures in the downscaled RCMs, which was in better
563 agreement with AWS observations, but was not present in the raw RCMs prior to downscaling. We note
564 that the downscaled maximum air temperature was at times higher than observations amongst all RCMs
565 during the post-monsoon and winter (Fig. A1) but the distribution of downscaled air temperatures was
566 similar to observed values (Fig. A2). Gamma-distribution quantile mapping substantially improved the
567 absolute precipitation values relative to the AWS observations compared to those in the raw RCMs; the
568 overestimation of winter precipitation and relative underestimation of monsoon precipitation amounts
569 in the raw RCMs was reduced and downscaled results show a clearer monsoon signal (Fig. A3). When
570 compared with AWS observations, RCM downscaling slightly overcorrected the seasonal precipitation
571 pattern with a slight underestimation of winter precipitation for the most extreme winter events. Across
572 the three present-day RCM simulations, the surface mass balance calculated using the NOAA RCM
573 was more positive than that for the ISPL and CCCma RCMs and most similar to the mass balance
574 calculated from meteorological observations, and remained the most positive mass balance in the end-
575 of-century time slices (Fig. 6).

576

577 **3.4 Evaluation of the iSOSIA glacier evolution model results**

578 COSIPY was used to calculate clean-ice surface mass balance from the downscaled RCMs, and the
579 insulating effects of supraglacial debris were calculated in iSOSIA. The simulated glacier geometry and
580 dynamics were compared with remotely sensed observations of ice thickness, supraglacial debris
581 distribution, velocity, and surface elevation change for the present-day glacier (Fig. 3) and varied
582 depending on the RCM used as forcing (Fig. 7). The experiment using the NOAA RCM was identified
583 as the starting point for all future simulations because this was most representative of the observed
584 glacier at 2015 CE (Fig. 3). The distributed surface mass balances calculated using COSIPY were most
585 similar to observed values after the calculated surface mass balances were integrated with the glacier
586 model to include accumulation by snow avalanching and the reduction in surface melting beneath
587 supraglacial debris; the active glacier extent was underestimated if supraglacial debris is not simulated
588 (Fig. 8). The supraglacial debris-mass balance feedback in the glacier model reproduced the observed
589 reversed mass balance gradient and peak in ablation below the Khumbu Icefall (Fig. 1D).

590

591 The simulated glacier area was 7.8 km^2 and similar to that obtained from structural mapping in 1979
592 CE (Nakawo, 1986). Radio-echo sounding in 1999 CE obtained ice thickness estimates close to the
593 active terminus of $\sim 160 \text{ m}$ (Gades et al., 2000) and simulated ice thickness at the terminus was 130 m
594 (Fig. 3A). The simulated thickness at the active glacier terminus thickness was approximately 175 m in
595 1999 CE, which agreed well with observations from DEMs of difference that show thinning here of up
596 to 55 m between 1984–2018 CE (Fig. 3D and 3E) (King et al., 2020). Simulated surface elevation
597 change in the ablation area was -30 m over 20 years to the present day and similar to values derived
598 from satellite observations for 1984–2018 CE (King et al., 2020). Simulated present-day glacier
599 velocities (Fig. 9) reached a maximum of 248 m a^{-1} and showed a similar pattern and magnitude to
600 glacier surface velocities observed using remote sensing observations, which reach a maximum of 220
601 m a^{-1} in the Khumbu Icefall (Altena and Käab, 2020) and up to 20 m a^{-1} in the ablation area (Quincey
602 et al., 2009; Dehecq et al. 2019). The simulated present-day velocities in this study were a better fit to

603 remote sensing observations than those from previous simulations that used an elevation-dependent
604 mass balance forcing (Rowan et al., 2015, 2021) where the maximum simulated velocities were 118 m
605 a^{-1} .

606

607 **3.5 Climate change and glacier evolution from the present day until 2100 CE**

608 Khumbu Glacier is responding to historical climate change and will continue to shrink even if warming
609 ceases today. Indeed, if we allow the spin-up experiment to reach equilibrium with the present-day
610 NOAA RCM mass balance, the glacier terminus will recede by 2.1 km and the maximum ice thickness
611 will decrease from 246 m to 206 m by 2100 CE without any additional warming. In this scenario, a
612 supraglacial debris layer up to 1.3 m thick extends 1 km up-glacier from the terminus and partially
613 dampens the committed volume loss, by sustaining 13% more ice volume than would be the possible
614 for a clean-ice glacier surface with the same mass balance (Fig. 10A). The committed glacier volume
615 loss due to historical warming in the absence of any further climate forcing is 10–23% of the present-
616 day glacier mass (Fig. 10C) with the associated uncertainty represented by this range of values arising
617 from the parameterisation of the impact of supraglacial debris evolution on surface melting.

618

619 Now considering the effects of additional warming under the RCP scenarios for the NOAA experiment,
620 we find that greater warming occurs in winter than in the monsoon under both RCPs and results in an
621 increase in annual precipitation amount of about 15% made up of a greater increase in non-monsoon
622 precipitation than monsoon precipitation (Fig. 2E). The climate forcing from the downscaled NOAA
623 RCM under RCP4.5 is 1.4°C warmer than the present day (-0.75°C in 2095–2100 CE compared with
624 -2.15°C in 2015–2020 CE) and annual precipitation increases by 14.8% from 581.4 mm at present day
625 to 664.8 mm a^{-1} by 2100 CE with monsoon (June–September) precipitation increasing by 5.4% and
626 non-monsoon season (December–February) precipitation increasing by 14.1% (Fig. 2E). Under
627 RCP8.5, the downscaled climate forcing is projected to be 3.8°C warmer than present day (1.65°C in
628 2095–2100 CE) with an increase in annual precipitation of 14.9% by 2100 CE, with monsoon
629 precipitation increasing by 9.8% and non-monsoon precipitation increasing by 19.4% (Fig. 2E).

630

631 In the NOAA RCM RCP4.5 experiment, the spatially averaged cumulative glacier mass balance is $-$
632 $0.14 \text{ m w.e. a}^{-1}$ in 2100 CE, which is slightly more positive than the present-day value of -0.21 m w.e.
633 a^{-1} (Fig. 6) and glacier volume decreases by 36% between the present day and 2100 CE (Fig. 10C).
634 While significant, this end-of-century glacier loss is partially offset by the concurrent increase in
635 precipitation. In comparison, an equivalent simulation forced only by warming and without any change
636 in precipitation results in a more linear trajectory of glacier change and 70% loss of glacier volume by
637 2100 CE (cyan line in Fig. 10C) demonstrating that 34% of potential glacier loss from warming could
638 be compensated by the increase in precipitation that occurs as a result of warming.

639

640 **3.6 Comparison of projections for different RCM forcings**

641 The CCCma and IPSL RCMs projected greater warming from the present day by 2100 CE than the
642 NOAA RCM under RCP4.5 with a value of 1.6°C ($+0.2^\circ\text{C}$ compared with the NOAA RCM) in the IPSL
643 RCM experiment and 2.2°C ($+0.8^\circ\text{C}$) in the CCCma RCM experiment. These two RCMs also projected
644 slightly greater warming by 2100 CE under RCP8.5, with a value of 3.9°C ($+0.1^\circ\text{C}$ compared with the
645 NOAA RCM) for the IPSL RCM experiment and 4.1°C ($+0.3^\circ\text{C}$) for the CCCma RCM experiment.

646

647 The projected increase in precipitation amount across the three RCMs is similar between RCPs with
648 annual totals above 600 mm by 2100 CE. The CCCma RCM gives the greatest increase in annual
649 precipitation amount of 100 mm by 2100 CE (Fig. 2E). There is no evidence of change in the intensity
650 of the Indian Summer Monsoon, as the seasonal split in precipitation remains similar to the present day,
651 but the frequency of days with high precipitation (over 15 mm per day) increases by 2100 CE, giving
652 twice as many days in the NOAA RCM experiment and up to seven times as many days in the IPSL
653 RCM experiment.

654

655 Under RCP8.5, all experiments showed similar results for mass balance by 2100 CE with only a 10%
656 difference in glacier volume between the three RCMs (Fig. 10C). The CCCma RCM experiment has
657 only a 1% difference in volume loss between RCP4.5 and RCP8.5 by 2100 CE despite a 1.9°C

658 difference in MAAT—this is a surprising result given the significant temperature difference, which can
659 be attributed to the greater number of high-magnitude precipitation events that occur under RCP8.5 in
660 combination with the small difference in winter temperatures between the two RCPs. Indeed, in the
661 CCCma RCM experiment under RCP4.5, the maximum winter temperature is 1.7°C higher than for the
662 other RCMs, resulting in ablation and rainfall (rather than snowfall) during the winter.
663

664 **4. Discussion**

665 **4.1 Uncertainties associated with the glacier modelling**

666 Sources of uncertainty in our results arose from each step of our glacier modelling workflow, and we
667 considered how the experiments could be designed to reduce these uncertainties. Here we discuss the
668 potential sources of uncertainty associated with the choice of RCMs, the downscaling of the RCMs, the
669 use of time slices rather than continuous mass balance calculations, the representation of future
670 precipitation in the RCMs, and the representation of avalanching in the glacier model.
671

672 A single RCM was not considered sufficient to represent both present-day climate and potential future
673 climatic extremes, but the climate-mass balance forcing ensemble was limited in size due to the small
674 number of RCMs available. The use of three RCMs allowed the implications of uncertainties in
675 understanding of local climate for glacier evolution to be evaluated. A multi-model mean approach
676 using all the CORDEX South Asia RCMs (as widely used elsewhere) was not considered sufficient to
677 represent present-day and future climate conditions in the Khumbu Valley because this approach gives
678 equal weighting to models irrespective of their performance (Pierce et al., 2009) and does not enable
679 intercomparison of results for future climate conditions.
680

681 Five-year downscaled RCM time slices were chosen to reduce computational expense associated with
682 COSIPY and the integration with iSOSIA. To ensure that the five-year periods selected were
683 representative, the preceding decade was used for comparison with the time-slice results (results not
684 shown). The use of quantile mapping with 14 years of AWS data as the downscaling method limited the
685 influence of any natural variability by ensuring that the period did not reflect an extreme phase of natural
686 climate oscillation. This comparison was particularly important for the future time slices, where large
687 uncertainties arise between RCMs, and observational data cannot be used for evaluation of the
688 downscaled climate or the resulting mass balance. We note that this experimental design could be
689 improved by interpolating the mass balance over time and coupling the COSIPY and iSOSIA models
690 such that mass balance was calculated dynamically for the evolving ice surface, but this was beyond
691 the scope of our experiments. However, the experiments were repeated using additional mid-Century
692 (2045–2050 CE) mass balance forcings to investigate if this produced a different end-of-Century result.
693 These experiments produced near-identical results in 2100 CE to the experiments with no mid-Century
694 forcing, in part because the response time of the simulated glaciers was longer than the 40-year period
695 between the present-day and future time slices. Thus, a mid-century surface mass balance forcing was
696 not considered necessary in our experiments and instead we used a step forcing for mass balance rather
697 than interpolation between mass balance calculations in the glacier model.
698

699 The differences in simulated glacier change and response time between RCM forcings were at times
700 greater than those resulting from the RCP due to differences in projections of precipitation. Whilst the
701 three selected RCMs performed well in representing annual precipitation cycles from the six available
702 CORDEX RCMs, we note that this representation was still fairly poor, although substantially improved
703 by quantile mapping (Fig. 2D). The poor representation of monsoon dynamics in the present-day RCMs
704 highlights an additional uncertainty associated with future precipitation scenarios and that these results
705 should be treated as a set of possible scenarios.
706

707 The CORDEX CMIP5 and CMIP6 projects only produced dynamically downscaled RCMs for two
708 future emissions scenarios (RCP4.5 and RCP8.5) and as such the implications of other RCPs for glacier
709 evolution could not be assessed. The downscaled future climates were compared with those from other
710 studies using CORDEX results, and showed similar annual and seasonal regional temperature trends
711 strongly linked to the choice of RCP, and similar positive precipitation trends with poor agreement
712 between RCMs (Kaini et al., 2019; Sanjay et al., 2017). The relationship between precipitation and

713 warming in the two future emissions scenarios was less clear than that for air temperatures because the
714 monsoon-influenced Himalaya has particularly poor RCM consensus and high levels of uncertainty in
715 future precipitation trends with warming relative to other regions in High Mountain Asia (Sanjay et al.,
716 2017).

717
718 A potentially large uncertainty in the glacier model arose from the parameterisation of avalanching, as
719 this mass balance variable is poorly constrained, with no direct observations of the avalanche
720 contribution to the mass balance of Khumbu Glacier and high regional variability (Kneib et al., 2025).
721 Avalanching was included in iSOSIA by slope-dependent diffusion and resulted in increased
722 accumulation along the glacier surface in the Western Cwm and improved the agreement between
723 simulated and estimated accumulation rates and distribution (Fig. 1D). Future work to resolve the
724 impact of low frequency–high magnitude avalanche events on accumulation rates would be useful to
725 refine this calculation but the contribution of avalanches to glacier accumulation over decadal time
726 scales remains extremely challenging to measure (Purdie et al., 2025).

727 728 **4.2 Impacts of mesoscale and microscale meteorology on glacier change**

729 Our study addresses fine-scale temporal (hourly) and spatial (100 m) glacier surface processes,
730 including avalanching and sublimation, that affect glacier surface mass balance across the elevation
731 range of Khumbu Glacier, but further observations of meteorological and glaciological conditions at
732 the highest elevations would be beneficial, and are needed if micro-scale processes are to be included
733 in glacier models (Brun et al., 2023; Khadka et al., 2021; Mölg et al., 2014; Shaw et al., 2022). Analysis
734 of meteorological observations from AWS across the Dudh Koshi catchment indicated that precipitation
735 gradients were weak, slightly negative or absent, confirming the observations of Salerno et al. (2015)
736 and Yang et al. (2017). To test the sensitivity of precipitation to elevation, COSIPY was forced by a
737 gridded climate distributed using weak negative, weak positive, and no precipitation gradients
738 distributed across the model domain using a linear regression with elevation from the 100-m resolution
739 DEM. The results of these experiments were used to force iSOSIA and the simulated historical glacier
740 evolution was similar, resulting in only a 10 m difference in the maximum ice thickness between
741 simulations with different precipitation gradients (result not shown).

742
743 The mass balance sensitivity to seasonal and daily variations in lapse rate showed a lesser impact on
744 glacier-wide mass balance than in other studies, due to the large elevation range of Khumbu Glacier
745 whereby a smaller fraction of the glacier relative to total area is located along the zero degree isotherm
746 (e.g., compared to Yala Glacier in Nepal; Immerzeel et al., 2014). Seasonal and daily lapse rates that
747 accounted for marked lower values during the monsoon season and at night gave a mean annual value
748 of $5.54\text{ }^{\circ}\text{C km}^{-1}$, which produced glacier-wide mass balance and ice thickness simulations that were
749 closest to geodetic observations and represented the maximum rates of surface lowering in the upper
750 ablation area where the debris layer is thinnest (Fig. 3D and 3E).

751
752 Sublimation simulated in our study occurred at all elevations with the highest rate of ice loss due to
753 sublimation ($-0.12\text{ m w.e. a}^{-1}$) in the upper reaches of the Khumbu Glacier catchment near to South Col
754 (about 7,495 m a.s.l.) where sublimation dominated ablation with only minor seasonality (Fig. A6).
755 Whilst this amount of ice loss by sublimation is not negligible, it is almost half that found in the point-
756 based calculations after adjusting for the different time periods represented by our studies (Matthews et
757 al., 2020), which is likely due to the assumed uniformity of wind speed across the model domain in
758 COSIPY. Future work to improve the calculation of sublimation in distributed surface mass balance
759 calculations for high-elevation glaciers would be valuable.

760
761 While we have considered the effects of mesoscale meteorology on glacier mass balance, smaller-scale
762 processes operating close to the land surface could also be important. Katabatic winds were suggested
763 to explain a local 15-year decrease in maximum air temperatures and precipitation over glaciers while
764 minimum air temperatures continued to rise (Salerno et al., 2023). However, this effect was found to be
765 short-lived (Shaw et al., 2025) and the impact of microscale near-surface cooling on the duration and
766 extent of mesoscale precipitation and accumulation is likely to be minimal and therefore unlikely to
767 significantly affect glacier-wide mass balance (Mott et al., 2020; Shaw et al., 2024). Observations from

768 the Camp 2 AWS (6,464 m a.s.l.) indicate that surface energy fluxes may be sufficient to cause non-
769 negligible melting of glacier surfaces despite freezing air temperatures (Matthews et al., 2020). Results
770 from an ice core from South Col Glacier (>8,000 m a.s.l.) combined with COSIPY experiments
771 suggested that ablation may also take place at even at the highest elevations (Potocki et al., 2022).
772 However, a subsequent study found no evidence of glacier mass change, and identified large
773 uncertainties associated with simulating mass balance at these extreme elevations where sub-daily air
774 temperature gradients and the duration of snow cover strongly affect ablation and accumulation (Brun
775 et al., 2023). Future work is needed to reduce these uncertainties, as very few observations exist of
776 accumulation processes and the upper limit of ablation processes for high-elevation Himalayan glaciers.
777

778 **4.3 Possible outcomes under RCP8.5**

779 Current global greenhouse gas emissions are following the trajectory of the intermediate emissions
780 scenario RCP4.5, while the high emissions scenario RCP8.5 could be described as ‘low possibility but
781 high impact’ (Pedersen et al., 2020). However, as represented in the RCMs used in our study, mountain
782 regions are warming more rapidly than the global mean such that a global temperature rise of 1.5°C will
783 lead to $2.1 \pm 0.1^\circ\text{C}$ of warming in High Mountain Asia (Kraaijenbrink et al., 2017; Pepin et al., 2022)
784 although the occurrence of elevation-dependent warming above 5,000 m a.s.l. is debated (Gao et al.,
785 2018). The high temperatures projected under RCP8.5 could potentially be offset partly by increased
786 precipitation, given that high-magnitude precipitation events from winter Westerly disturbances
787 increased by a factor of seven between present day and 2100 CE in the IPSL RCM under RCP8.5.
788

789 We found no evidence of future increases in precipitation offsetting RCP8.5 warming; net glacier mass
790 balance was strongly negative in all RCP8.5 experiments and insufficient to maintain any actively
791 flowing glacier. Under RCP8.5, glacier mass balance in the monsoon-influenced Himalaya may
792 therefore shift from being driven by accumulation during the monsoon to predominantly during winter.
793 Monsoon precipitation would only result in snow accumulation at the very highest elevations and would
794 be insufficient to maintain flowing glaciers. This outcome is avoidable by limiting anthropogenic
795 warming to within RCP4.5, which, due to the associated increase in precipitation, could sustain nearly
796 two thirds of the current glacier volume until 2100 CE and potentially for two centuries further into the
797 future.
798

799 **4.4 Comparison with global glacier modelling results**

800 A recent global glacier modelling study forced by an ensemble of 10 GCMs projected mass loss of 64%
801 for Khumbu Glacier by 2100 CE (Rounce et al., 2023). In comparison, our experiments project less
802 severe rates of decline, resulting in 30% less mass loss under the RCP4.5 future climate scenario than
803 in the global study (Fig. 10C). One difference between these results is that rather than using the global
804 glacier inventory outline to define the glacier margins we consider only the actively flowing glacier and
805 so exclude 20% of the starting glacier volume in the detached tongue. We would expect the two sections
806 of the glacier to evolve along different paths; while the active glacier responds to climate change as
807 projected in our experiments, thick supraglacial debris mantling the detached tongue could allow this
808 ice mass to survive and slowly decay *in situ* for many decades beyond the present day. The decay of the
809 detached tongue may however increase due to erosion of the surface by ice cliffs and supraglacial water
810 bodies that are expanding across the former glacier surface (King et al., 2020).
811

812 Our experiments only consider the rapidly changing active glacier, and we expect that the debris-
813 covered tongue would melt more slowly than projected in the global modelling study, but as we do not
814 consider the stagnant tongue to be part of the present-day glacier the ice volume simulated at the start
815 of our experiments is smaller than that represented by Rounce et al. (2023) and other studies based on
816 the RGI glacier inventory. The dynamically detached debris-covered tongue represents about 20% of
817 the present-day glacier volume and contains ice estimated as up to 360 m thick. The mean present-day
818 ablation rate across this section of the glacier simulated in Rowan et al. (2021) is $-0.54 \text{ m.w.e. a}^{-1}$ which
819 can be used to estimate the life expectancy of the debris-covered tongue assuming no input of ice from
820 the active glacier and no change in ablation rate due to thickening of supraglacial debris or the
821 development of ice cliffs and supraglacial ponds. While the thickest part of the detached tongue may

822 survive for ~600 years, the mean life expectancy of this ice mass is 176 ± 148 years from the present
823 day meaning that the former debris-covered tongue will vanish by 2200 CE.

824

825 **4.5 The response of large debris-covered glaciers to climate change**

826 The dynamic response time of large glaciers to climate change is of the order of centuries. For this
827 reason, we start our simulations from the late Holocene (~1 ka) moraine extent when Khumbu Glacier
828 was last considered dynamically stable (Hornsey et al., 2022; Rowan et al., 2015). The relationship
829 between glacier response time and mass balance becomes less important after 2100 CE when the glacier
830 is so small that ice flow has little impact on glacier volume change. Global and regional glacier
831 modelling studies typically start their simulations in the current Century (e.g., 2000–2007 CE in
832 Marzeion et al. (2020); 2000 CE in Rounce et al. (2023)) and a further complication arises from the use
833 of global glacier inventories as a starting point for glacier modelling studies as such inventories cannot
834 capture the current dynamic state of glaciers that are imbalanced, and include all ice-covered areas
835 rather than identifying only actively flowing ice. However, satellite-derived velocity products could be
836 used identify where ice flow within glacier outlines declines to negligible rates (Dehecq et al., 2019).

837

838 The RGI 7.0 inventory for Khumbu Glacier is based on imagery from 1999 CE (RGI 7.0 Consortium,
839 2023) where the detached debris-covered tongue represents 20% of the glacier volume contained within
840 this outline (Fig. 1C). Simulations that integrated the stagnant tongue into the model domain rather than
841 as part of the flowing ice improved the representation of simulated ice flow compared to observed
842 values, supporting our conclusion that the debris-covered tongue has been dynamically detached from
843 the active glacier for 50–100 years (Rowan et al., 2021). Field observations support the concept of
844 active and stagnant sections co-existing in contact with each other as englacial optical televiewing
845 indicated that thrusting occurs at several sites, denoted by skewed internal debris layers and of basal ice
846 that has been thrust to the glacier surface, near to the active glacier terminus from the direction of
847 Khumbu Icefall (Miles et al., 2021). Our simulations show that development of supraglacial debris at
848 the active glacier terminus reduced net volume loss by 13% (Fig. 8). Dynamic detachment of debris-
849 covered tongues could allow these glaciers to move closer to equilibrium with a rapidly changing
850 climate, the local mass balance gradient is a more important control on glacier change for both clean-
851 ice glaciers and debris-covered Himalayan glaciers.

852

853 **5. Conclusions**

854 In the monsoon-influenced Himalaya, 85% of the glacier area is located higher than 5,000 m above sea
855 level, and 21% of this ice is above 6000 m in elevation. Despite these high elevations, Himalayan
856 glaciers are rapidly losing ice in response to recent warming and are projected to shrink by 53% to 70%
857 during this Century. However, the impact of future changes in precipitation on glacier loss remains
858 uncertain, because changes in precipitation amount and distribution is often overlooked in glacier model
859 projections. We explored the effects of future warming in tandem with changes in precipitation by
860 simulating the evolution of Khumbu Glacier in the Everest region of Nepal using a surface energy and
861 mass balance model forced by downscaled Regional Climate Model outputs to drive an ice-dynamical
862 glacier evolution model. Historical warming commits Khumbu Glacier to loss of 10–23% of the total
863 ice volume by 2100 CE. While warming due to intermediate future greenhouse gas emissions (RCP4.5)
864 will lead to glacier volume loss of 70% by 2100 CE, the projected concurrent increase in precipitation
865 amount will offset 34% of this and so reduce glacier loss by about a half. However, high future
866 emissions (RCP8.5) will not be compensated by changes in precipitation amount but will instead result
867 in substantial ablation above 6,000 m with devastating consequences for one of the highest glaciers on
868 Earth. Our results indicate that the net mass balance of Khumbu Glacier could be close to zero in 2100
869 CE under RCP4.5 and therefore, if climate change is limited to this intermediate emissions scenario,
870 Khumbu Glacier will recede to the base of the icefall with insignificant further change in glacier volume
871 beyond this point. In this scenario, Khumbu Glacier has a similar extent in 2100 CE to the active section
872 of the present-day glacier, and represents at least one example of how monsoon-influenced Himalayan
873 glaciers could persist into the future if global efforts are sufficient to mitigate anthropogenic climate
874 change.

875

876

877 **Code availability**

878 The COSIPY version 1.3 glacier surface energy and mass balance model is available from the original
879 publication describing this model (Sauter et al., 2020) and Zenodo (Arndt et al., 2020). The iSOSIA
880 version spm-3.3.3r glacier model is available from Zenodo (Rowan and Pedersen, 2024).

881

882 **Data availability**

883 Daily data from the Coordinated Regional Downscaling Experiment (CORDEX) South Asia domain
884 were downloaded from the Indian Institute of Tropical Meteorology website
885 (http://cccr.tropmet.res.in/home/cordexsa_about.jsp) for the grid box nearest to Khumbu Glacier
886 (27.9065°N, 86.4353°E). Incoming shortwave and longwave radiation components were downloaded
887 from the ESGF portal (<https://esgf-ui.ceda.ac.uk/cog/projects/cordex-ceda/>). Meteorological
888 observations were derived from the Ev-K2-CNR SHARE network (<https://www.evk2cnr.org>) and the
889 GlacioClim (<https://glacioclim.osug.fr/>).

890

891 **Author contributions**

892 Conceptualisation: DJQ, ANR, AVR

893 Data curation: ASD, ANR, AVR

894 Formal analysis: ASD, ANR, AVR

895 Funding acquisition: DJQ, ANR, AVR

896 Investigation: ASD

897 Methodology: ASD, ANR, AVR, VKP

898 Project administration: DJQ, ANR

899 Resources: DJQ, ANR

900 Software: AVR, VKP

901 Supervision: DJQ, ANR, AVR

902 Validation: ASD, AVR

903 Visualisation: ASD, AVR

904 Writing – original draft preparation: ASD, AVR, DJQ, ANR, VKP

905 Writing – review and editing: ASD, AVR, DJQ, ANR, VKP

906

907 **Competing interests**

908 The authors declare that they have no conflicts of interest related to this work.

909

910 **Acknowledgements**

911 Tobias Sauter and Anselm Arndt are thanked for support in using COSIPY. We thank Patrick Wagon
912 for sharing the Pyramid and Changri Nup Glacier automatic weather station data. We thank David
913 Rounce for sharing the global glacier model results for Khumbu Glacier from Rounce et al. (2023). We
914 thank Editor Emily Collier, Emily Potter and an anonymous reviewer for their detailed and constructive
915 comments that greatly improved the focus and clarity of this work.

916

917 **Financial support**

918 ASD was supported by the Priestley International Centre for Climate at the University of Leeds, and a
919 University of Leeds Anniversary Research Scholarship. AVR was supported by a Royal Society
920 Dorothy Hodgkin Research Fellowship (DHF\R1\201113). Some of the simulations presented were
921 performed using resources provided by Sigma2, the National Infrastructure for High-Performance
922 Computing and Data Storage in Norway.

923

924

925 **References**

926 Altena, B. and Käab, A.: Ensemble matching of repeat satellite images applied to measure fast-changing
927 ice flow, verified with mountain climber trajectories on Khumbu icefall, Mount Everest, J.
928 Glaciol., 66, 905–915, <https://doi.org/10.1017/jog.2020.66>, 2020

929 Arndt, A., Sauter, T., Saß, B.: cryotools/cosipy: COSIPY v1.3 – An open-source coupled snowpack and
930 ice surface energy and mass balance model (v1.3). Zenodo.
931 <https://doi.org/10.5281/zenodo.3902191>, 2020

- 932 Anderson, L. S. and Anderson, R. S.: Modeling debris-covered glaciers: response to steady debris
933 deposition, *The Cryosphere*, 10, 1105–1124, <https://doi.org/10.5194/tc-10-1105-2016>, 2016
- 934 Bartlett, O. T., Ng, F. S. L., and Rowan, A. V.: Morphology and evolution of supraglacial hummocks on
935 debris-covered Himalayan glaciers, *Earth Surf. Process. Landforms*, 46, 525–539,
936 <https://doi.org/10.1002/esp.5043>, 2021
- 937 Benn, D. I. and Lehmkuhl, F.: Mass balance and equilibrium-line altitudes of glaciers in high-mountain
938 environments, *Quaternary International*, 65–66, 15–29, [https://doi.org/10.1016/S1040-6182\(99\)00034-8](https://doi.org/10.1016/S1040-6182(99)00034-8), 2000
- 940 Benn, D. I. and Owen, L. A.: The role of the Indian summer monsoon and the mid-latitude westerlies
941 in Himalayan glaciation: review and speculative discussion, *Journal of the Geological Society*,
942 155, 353–363, <https://doi.org/10.1144/gsjgs.155.2.0353>, 1998
- 943 Biemans, L.H. Speelman, F. Ludwig, E.J. Moors, A.J. Wiltshire, P. Kumar, D. Gerten, P., Kabat, P.:
944 Future water resources for food production in five South Asian river basins and potential for
945 adaptation—A modeling study, *Science of The Total Environment*,
946 <https://doi.org/10.1016/j.scitotenv.2013.05.092>, 2013
- 947 Bonekamp, P. N. J., Wanders, N., Wiel, K., Lutz, A. F., Immerzeel, W. W.: Using large ensemble
948 modelling to derive future changes in mountain specific climate indicators in a 2 and 3°C warmer
949 world in High Mountain Asia, *Int J Climatol*, 41, <https://doi.org/10.1002/joc.6742>, 2021
- 950 Bookhagen, B. and Burbank, D. W.: Topography, relief, and TRMM-derived rainfall variations along
951 the Himalaya, *Geophys. Res. Lett.*, 33, L08405, <https://doi.org/10.1029/2006GL026037>, 2006
- 952 Brock, B.W., Willis, I.C. and Sharp, M.J.: Measurement and parameterization of aerodynamic
953 roughness length variations at Haut Glacier d’Arolla, Switzerland. *Journal of Glaciology*,
954 52(177), pp.281–297. <https://doi.org/10.3189/172756506781828746>, 2006
- 955 Brun, F., King, O., Réveillet, M., Amory, C., Planchot, A., Berthier, E., Dehecq, A., Bolch, T., Fourteau,
956 K., Brondex, J., Dumont, M., Mayer, C., Leinss, S., Hugonnet, R., and Wagnon, P.: Everest South
957 Col Glacier did not thin during the period 1984–2017, *The Cryosphere*, 17, 3251–3268,
958 <https://doi.org/10.5194/tc-17-3251-2023>, 2023
- 959 Collins, M., Knutti, R., and Arblaster, J.: Long-term Climate Change: Projections, Commitments and
960 Irreversibility. In: *Climate Change 2013: The Physical Science Basis. Contribution of Working
961 Group I to the Fifth Assessment Report of the Intergovernmental Panel on Climate Change*
962 [Stocker, T.F., D. Qin, G.-K. Plattner, M. Tignor, S.K. Allen, J. Boschung, A. Nauels, Y. Xia, V.
963 Bex and P.M. Midgley (eds.)]. Cambridge University Press, Cambridge, United Kingdom and
964 New York, NY, USA., 1–108., 2013
- 965 Compagno, L., Huss, M., Miles, E. S., McCarthy, M. J., Zekollari, H., Dehecq, A., Pellicciotti, F., and
966 Farinotti, D.: Modelling supraglacial debris-cover evolution from the single-glacier to the
967 regional scale: an application to High Mountain Asia, *The Cryosphere*, 16, 1697–1718,
968 <https://doi.org/10.5194/tc-16-1697-2022>, 2022
- 969 Cuffey, K.M. and Paterson, W.S.B.: *The physics of glaciers*. Academic Press, 2010
- 970 Dehecq, A., Gourmelen, N., Gardner, A. S., Brun, F., Goldberg, D., Nienow, P. W., Berthier, E., Vincent,
971 C., Wagnon, P., and Trouvé, E.: Twenty-first century glacier slowdown driven by mass loss in
972 High Mountain Asia, *Nature Geosci*, 12, 22–27, <https://doi.org/10.1038/s41561-018-0271-9>,
973 2019
- 974 Egholm, D. L., Knudsen, M. F., Clark, C. D., and Lesemann, J. E.: Modeling the flow of glaciers in
975 steep terrains: The integrated second-order shallow ice approximation (iSOSIA), *J. Geophys.
976 Res.*, 116, <https://doi.org/10.1029/2010JF001900>, 2011
- 977 Farinotti, D., Huss, M., Fürst, J. J., Landmann, J., Machguth, H., Maussion, F., and Pandit, A.: A
978 consensus estimate for the ice thickness distribution of all glaciers on Earth, *Nat. Geosci.*, 12,
979 168–173, <https://doi.org/10.1038/s41561-019-0300-3>, 2019
- 980 Farr, T. G., Rosen, P. A., Caro, E., Crippen, R., Duren, R., Hensley, S., Kobrick, M., Paller, M.,
981 Rodriguez, E., Roth, L., Seal, D., Shaffer, S., Shimada, J., Umland, J., Werner, M., Oskin, M.,
982 Burbank, D., and Alsdorf, D.: The Shuttle Radar Topography Mission, *Reviews of Geophysics*,
983 45, 2005RG000183, <https://doi.org/10.1029/2005RG000183>, 2007
- 984 Ferguson, J. and Vieli, A.: Modelling steady states and the transient response of debris-covered glaciers,
985 *Cryosphere*, <https://doi.org/10.5194/tc-2020-228>, 2020

- 986 Förster, K., Hanzer, F., Winter, B., Marke, T., and Strasser, U.: An open-source MEteoroLOGical
987 observation time series DISaggregation Tool (MELODIST v0.1.1), *Geosci. Model Dev.*, 9, 2315–
988 2333, <https://doi.org/10.5194/gmd-9-2315-2016>, 2016
- 989 Gades, A., Conway, H., Nereson, N., Naito, N., and Kadota, T.: Radio echo-sounding through
990 supraglacial debris on Lirung and Khumbu Glaciers, Nepal Himalayas, Debris-Covered Glaciers
991 (Proceedings of a workshop held at Seattle, Washington, USA, September 2000). *IAHS*, 264, 13–
992 22, 2000
- 993 Gao, Y., Chen, F., Lettenmaier, D. P., Xu, J., Xiao, L., and Li, X.: Does elevation-dependent warming
994 hold true above 5000 m elevation? Lessons from the Tibetan Plateau, *npj Clim Atmos Sci*, 1, 19,
995 <https://doi.org/10.1038/s41612-018-0030-z>, 2018
- 996 Gromke, C., Manes, C., Walter, B., Lehning, M. and Guala, M.: Aerodynamic roughness length of fresh
997 snow. *Boundary-Layer Meteorology*, 141, pp.21-34. <https://doi.org/10.1007/s10546-011-9623-3>,
998 2011
- 999 Guo, S., Chen, R., Liu, G., Han, C., Song, Y., Liu, J., Yang, Y., Liu, Z., Wang, X., Liu, X. and Wang, L.:
1000 Simple parameterization of aerodynamic roughness lengths and the turbulent heat fluxes at the
1001 top of midlatitude August-One Glacier, Qilian Mountains, China. *Journal of Geophysical*
1002 *Research: Atmospheres*, 123(21), pp.12-066. <https://doi.org/10.1029/2018JD028875>, 2018
- 1003 Herreid, S. and Pellicciotti, F.: The state of rock debris covering Earth’s glaciers, *Nat. Geosci.*, 13, 621–
1004 627, <https://doi.org/10.1038/s41561-020-0615-0>, 2020
- 1005 Hornsey, J., Rowan, A. V., Kirkbride, M. P., Livingstone, S. J., Fabel, D., Rodes, A., Quincey, D. J.,
1006 Hubbard, B., and Jomelli, V.: Be-10 Dating of Ice-Marginal Moraines in the Khumbu Valley,
1007 Nepal, Central Himalaya, Reveals the Response of Monsoon-Influenced Glaciers to Holocene
1008 Climate Change, *JGR Earth Surface*, 127, <https://doi.org/10.1029/2022JF006645>, 2022
- 1009 Huintjes, E., Neckel, N., Hochschild, V., and Schneider, C.: Surface energy and mass balance at
1010 Purogangri ice cap, central Tibetan Plateau, 2001–2011, *J. Glaciol.*, 61, 1048–1060,
1011 <https://doi.org/10.3189/2015JoG15J056>, 2015
- 1012 Immerzeel, W. W., van Beek, L. P. H., Konz, M., Shrestha, A. B., and Bierkens, M. F. P.: Hydrological
1013 response to climate change in a glacierized catchment in the Himalayas, *Climatic Change*, 110,
1014 721–736, <https://doi.org/10.1007/s10584-011-0143-4>, 2012
- 1015 Irvine-Fynn, T.D., Sanz-Ablanedo, E., Rutter, N., Smith, M.W. and Chandler, J.H.: Measuring glacier
1016 surface roughness using plot-scale, close-range digital photogrammetry. *Journal of Glaciology*,
1017 60(223), pp.957-969. doi:10.3189/2014JoG14J032, 2014
- 1018 Jouvét, G., Huss, M., Funk, M., and Blatter, H.: Modelling the retreat of Grosser Aletschgletscher,
1019 Switzerland, in a changing climate, *J. Glaciol.*, 57, 1033–1045,
1020 <https://doi.org/10.3189/002214311798843359>, 2011
- 1021 Kaini, S., Nepal, S., Pradhananga, S., Gardner, T. and Sharma, A. K.: Representative general circulation
1022 models selection and downscaling of climate data for the transboundary Koshi river basin in
1023 China and Nepal. *International Journal of Climatology*, 40(9): 4131-4149. doi: 10.1002/joc.6447,
1024 2019
- 1025 Katzenberger, A., Schewe, J., Pongratz, J., and Levermann, A.: Robust increase of Indian monsoon
1026 rainfall and its variability under future warming in CMIP6 models, *Earth Syst. Dynam.*, 12, 367–
1027 386, <https://doi.org/10.5194/esd-12-367-2021>, 2021.
- 1028 Khadka, A., Matthews, T., Perry, L. B., Koch, I., Wagnon, P., Shrestha, D., Sherpa, T. C., Aryal, D., Tait,
1029 A., Sherpa, T. G., Tuladhar, S., Baidya, S. K., Elvin, S., Elmore, A. C., Gajurel, A., and Mayewski,
1030 P. A.: Weather On Mount Everest During The 2019 Summer Monsoon, *Weather*, 76, 205–207,
1031 <https://doi.org/10.1002/wea.3931>, 2021.
- 1032 King, O., Bhattacharya, A., Ghuffar, S., Tait, A., Guilford, S., Elmore, A. C., and Bolch, T.: Six Decades
1033 of Glacier Mass Changes around Mt. Everest Are Revealed by Historical and Contemporary
1034 Images, *One Earth*, 3, 608–620, <https://doi.org/10.1016/j.oneear.2020.10.019>, 2020.
- 1035 Knap, W.H. and Oerlemans, J.: The surface albedo of the Greenland ice sheet: satellite-derived and in
1036 situ measurements in the Søndre Strømfjord area during the 1991 melt season. *Journal of*
1037 *Glaciology*, 42(141), pp.364-374. doi:10.3189/S002214300004214, 1996
- 1038 Kneib, M., Maussion, F., Brun, F., Carcanade, G., Farinotti, D., Huss, M., Van Tiel, M., Jouberton, A.,
1039 Schmitt, P., Schuster, L., Dehecq, A., and Champollion, N.: Topographically-controlled

1040 contribution of avalanches to glacier mass balance in the 21st century, *Nat Commun*, 16, 10122,
1041 <https://doi.org/10.1038/s41467-025-65608-z>, 2025.

1042 Kraaijenbrink, P. D. A., Bierkens, M. F. P., Lutz, A. F., and Immerzeel, W. W.: Impact of a global
1043 temperature rise of 1.5 degrees Celsius on Asia's glaciers, *Nature*, 549, 257–260,
1044 <https://doi.org/10.1038/nature23878>, 2017.

1045 Lafon, T., Dadson, S., Buys, G. and Prudhomme, C.: Bias correction of daily precipitation simulated by
1046 a regional climate model: a comparison of methods. *International journal of climatology*, 33(6),
1047 pp.1367-1381, 2013

1048 Laha, S., Kumari, R., Singh, S., Mishra, A., Sharma, T., Banerjee, A., Nainwal, H. C., and Shankar, R.:
1049 Evaluating the contribution of avalanching to the mass balance of Himalayan glaciers, *Ann.*
1050 *Glaciol.*, 58, 110–118, <https://doi.org/10.1017/aog.2017.27>, 2017.

1051 Luo, M., Liu, T., Meng, F., Duan, Y., Frankl, A., Bao, A. and De Maeyer, P.: Comparing bias correction
1052 methods used in downscaling precipitation and temperature from regional climate models: A case
1053 study from the Kaidu River basin in western China. *Water*. 10(8), pp. 1046.
1054 <https://doi.org/10.3390/w10081046>, 2018

1055 Lutz, A.F., Immerzeel, W.W., Kraaijenbrink, P.D., Shrestha, A.B. and Bierkens, M.F.: Climate change
1056 impacts on the upper Indus hydrology: sources, shifts and extremes. *PloS one*, 11(11),
1057 p.e0165630, 2016

1058 Marzeion, B., Hock, R., Anderson, B., Bliss, A., Champollion, N., Fujita, K., Huss, M., Immerzeel, W.
1059 W., Kraaijenbrink, P., Malles, J., Maussion, F., Radić, V., Rounce, D. R., Sakai, A., Shannon, S.,
1060 Van De Wal, R., and Zekollari, H.: Partitioning the Uncertainty of Ensemble Projections of
1061 Global Glacier Mass Change, *Earth's Future*, 8, e2019EF001470,
1062 <https://doi.org/10.1029/2019EF001470>, 2020.

1063 Maraun, D.: Bias correcting climate change simulations-a critical review. *Current Climate Change*
1064 *Reports*, 2(4), pp.211-220, 2016

1065 Matthews, T., Perry, L. B., Koch, I., Aryal, D., Khadka, A., Shrestha, D., Abernathy, K., Elmore, A. C.,
1066 Seimon, A., Tait, A., Elvin, S., Tuladhar, S., Baidya, S. K., Potocki, M., Birkel, S. D., Kang, S.,
1067 Sherpa, T. C., Gajurel, A., and Mayewski, P. A.: Going to Extremes: Installing the World's
1068 Highest Weather Stations on Mount Everest, *Bulletin of the American Meteorological Society*,
1069 101, E1870–E1890, <https://doi.org/10.1175/BAMS-D-19-0198.1>, 2020.

1070 Maurer, J. M., Schaefer, J. M., Rupper, S., and Corley, A.: Acceleration of ice loss across the Himalayas
1071 over the past 40 years, *Sci. Adv.*, 5, eaav7266, <https://doi.org/10.1126/sciadv.aav7266>, 2019.

1072 Miles, E. S., Willis, I., Buri, P., Steiner, J. F., Arnold, N. S., and Pellicciotti, F.: Surface Pond Energy
1073 Absorption Across Four Himalayan Glaciers Accounts for 1/8 of Total Catchment Ice Loss,
1074 *Geophys. Res. Lett.*, 45, <https://doi.org/10.1029/2018GL079678>, 2018a.

1075 Miles, K. E., Hubbard, B., Quincey, D. J., Miles, E. S., Sherpa, T. C., Rowan, A. V., and Doyle, S. H.:
1076 Polythermal structure of a Himalayan debris-covered glacier revealed by borehole thermometry,
1077 *Sci Rep*, 8, 16825, <https://doi.org/10.1038/s41598-018-34327-5>, 2018b.

1078 Miles, K. E., Hubbard, B., Miles, E. S., Quincey, D. J., Rowan, A. V., Kirkbride, M., and Hornsey, J.:
1079 Continuous borehole optical televiewing reveals variable englacial debris concentrations at
1080 Khumbu Glacier, Nepal, *Commun Earth Environ*, 2, 12, [https://doi.org/10.1038/s43247-020-](https://doi.org/10.1038/s43247-020-00070-x)
1081 [00070-x](https://doi.org/10.1038/s43247-020-00070-x), 2021.

1082 Miles, K. E., Hubbard, B., Miles, E. S., Quincey, D. J., and Rowan, A. V.: Internal structure of a
1083 Himalayan debris-covered glacier revealed by borehole optical televiewing, *J. Glaciol.*, 1–12,
1084 <https://doi.org/10.1017/jog.2022.100>, 2022.

1085 Mölg, T., Maussion, F., Yang, W. and Scherer, D.: The footprint of Asian monsoon dynamics in the mass
1086 and energy balance of a Tibetan glacier. *The Cryosphere*, 6(6), pp.1445-1461.
1087 <https://doi.org/10.5194/tc-6-1445-2012>, 2012

1088 Mölg, T., Maussion, F., and Scherer, D.: Mid-latitude westerlies as a driver of glacier variability in
1089 monsoonal High Asia, *Nature Clim Change*, 4, 68–73, <https://doi.org/10.1038/nclimate2055>,
1090 2014.

1091 Mott, R., Stiperski, I., and Nicholson, L.: Spatio-temporal flow variations driving heat exchange
1092 processes at a mountain glacier, *The Cryosphere*, 14, 4699–4718, [https://doi.org/10.5194/tc-14-](https://doi.org/10.5194/tc-14-4699-2020)
1093 [4699-2020](https://doi.org/10.5194/tc-14-4699-2020), 2020.

- 1094 Nakawo, M.: Processes Which Distribute Supraglacial Debris On The Khumbu Glacier, Nepal
 1095 Himalaya, *Annals of Glaciology*, 8, 1986.
- 1096 Nicholson, L., Wirbel, A., Mayer, C., and Lambrecht, A.: The Challenge of Non-Stationary Feedbacks
 1097 in Modeling the Response of Debris-Covered Glaciers to Climate Forcing, *Front. Earth Sci.*, 9,
 1098 662695, <https://doi.org/10.3389/feart.2021.662695>, 2021.
- 1099 Oerlemans, J.: *Glaciers and climate change*. CRC Press, 2001
- 1100 Owen, L. A., Robinson, R., Benn, D. I., Finkel, R. C., Davis, N. K., Yi, C., Putkonen, J., Li, D., and
 1101 Murray, A. S.: Quaternary glaciation of Mount Everest, *Quaternary Science Reviews*, 28, 1412–
 1102 1433, <https://doi.org/10.1016/j.quascirev.2009.02.010>, 2009.
- 1103 Pedersen, J. S. T., Van Vuuren, D. P., Aparício, B. A., Swart, R., Gupta, J., and Santos, F. D.: Variability
 1104 in historical emissions trends suggests a need for a wide range of global scenarios and regional
 1105 analyses, *Commun Earth Environ*, 1, 41, <https://doi.org/10.1038/s43247-020-00045-y>, 2020.
- 1106 Pellicciotti, F., Stephan, C., Miles, E., Herreid, S., Immerzeel, W. W., and Bolch, T.: Mass-balance
 1107 changes of the debris-covered glaciers in the Langtang Himal, Nepal, from 1974 to 1999, *J.*
 1108 *Glaciol.*, 61, 373–386, <https://doi.org/10.3189/2015JoG13J237>, 2015.
- 1109 Pepin, N. C., Arnone, E., Gobiet, A., Haslinger, K., Kotlarski, S., Notarnicola, C., Palazzi, E., Seibert,
 1110 P., Serafin, S., Schöner, W., Terzago, S., Thornton, J. M., Vuille, M., and Adler, C.: Climate
 1111 Changes and Their Elevational Patterns in the Mountains of the World, *Reviews of Geophysics*,
 1112 60, <https://doi.org/10.1029/2020RG000730>, 2022.
- 1113 Piani, C., Weedon, G.P., Best, M., Gomes, S.M., Viterbo, P., Hagemann, S. and Haerter, J.O.: Statistical
 1114 bias correction of global simulated daily precipitation and temperature for the application of
 1115 hydrological models. *Journal of hydrology*, 395(3-4), pp.199-215.
 1116 <https://doi.org/10.1016/j.jhydrol.2010.10.024>, 2010
- 1117 Pierce, D. W., Barnett, T. P., Santer, B. D., and Gleckler, P. J.: Selecting global climate models for
 1118 regional climate change studies, *Proc. Natl. Acad. Sci. U.S.A.*, 106, 8441–8446,
 1119 <https://doi.org/10.1073/pnas.0900094106>, 2009.
- 1120 Potocki, M., Mayewski, P. A., Matthews, T., Perry, L. B., Schwikowski, M., Tait, A. M., Korotkikh, E.,
 1121 Clifford, H., Kang, S., Sherpa, T. C., Singh, P. K., Koch, I., and Birkel, S.: Mt. Everest’s highest
 1122 glacier is a sentinel for accelerating ice loss, *npj Clim Atmos Sci*, 5, 7,
 1123 <https://doi.org/10.1038/s41612-022-00230-0>, 2022.
- 1124 Pritchard, H. D.: Asia’s shrinking glaciers protect large populations from drought stress, *Nature*, 569,
 1125 649–654, <https://doi.org/10.1038/s41586-019-1240-1>, 2019.
- 1126 Purdie, H., Kerr, T., Robson, B., Anderson, B., Lorrey, A. M., Rack, W., Brasington, J., and Bealing, P.:
 1127 Mass balance characteristics of the ‘vanishing’ Rolleston Glacier, New Zealand, *Ann. Glaciol.*,
 1128 66, e31, <https://doi.org/10.1017/aog.2025.10032>, 2025.
- 1129 Quincey, D. J., Luckman, A., and Benn, D.: Quantification of Everest region glacier velocities between
 1130 1992 and 2002, using satellite radar interferometry and feature tracking, *J. Glaciol.*, 55, 596–606,
 1131 <https://doi.org/10.3189/002214309789470987>, 2009.
- 1132 Ragettli, S., Immerzeel, W. W., and Pellicciotti, F.: Contrasting climate change impact on river flows
 1133 from high-altitude catchments in the Himalayan and Andes Mountains, *Proc Natl Acad Sci USA*,
 1134 113, 9222–9227, <https://doi.org/10.1073/pnas.1606526113>, 2016.
- 1135 RGI 7.0 Consortium: A Dataset of Global Glacier Outlines, Version 7.0. Boulder, Colorado USA.
 1136 NSIDC: National Snow and Ice Data Center, <https://doi.org/10.5067/f6jmovy5navz>, 2023.
- 1137 Reiter, P., Gutjahr, O., Schefczyk, L., Heinemann, G. and Casper, M.: Does applying quantile mapping
 1138 to subsamples improve the bias correction of daily precipitation?. *International Journal of*
 1139 *Climatology*, 38(4), pp.1623-1633, 2018
- 1140 Roering, J. J., Kirchner, J. W., and Dietrich, W. E.: Evidence for nonlinear, diffusive sediment transport
 1141 on hillslopes and implications for landscape morphology, *Water Resources Research*, 35, 853–
 1142 870, <https://doi.org/10.1029/1998WR900090>, 1999.
- 1143 Rounce, D. R., Hock, R., Maussion, F., Hugonnet, R., Kochtitzky, W., Huss, M., Berthier, E.,
 1144 Brinkerhoff, D., Compagno, L., Copland, L., Farinotti, D., Menounos, B., and McNabb, R. W.:
 1145 Global glacier change in the 21st century: Every increase in temperature matters, *Science*, 379,
 1146 78–83, <https://doi.org/10.1126/science.abo1324>, 2023.

- 1147 Rowan, A. V.: The ‘Little Ice Age’ in the Himalaya: A review of glacier advance driven by Northern
 1148 Hemisphere temperature change, *The Holocene*, 27, 292–308,
 1149 <https://doi.org/10.1177/0959683616658530>, 2017.
- 1150 Rowan, A. V., Egholm, D. L., Quincey, D. J., and Glasser, N. F.: Modelling the feedbacks between mass
 1151 balance, ice flow and debris transport to predict the response to climate change of debris-covered
 1152 glaciers in the Himalaya, *Earth and Planetary Science Letters*, 430, 427–438,
 1153 <https://doi.org/10.1016/j.epsl.2015.09.004>, 2015.
- 1154 Rowan, A. V., Egholm, D. L., Quincey, D. J., Hubbard, B., King, O., Miles, E. S., Miles, K. E., and
 1155 Hornsey, J.: The Role of Differential Ablation and Dynamic Detachment in Driving Accelerating
 1156 Mass Loss From a Debris-Covered Himalayan Glacier, *J. Geophys. Res. Earth Surf.*, 126,
 1157 <https://doi.org/10.1029/2020JF005761>, 2021.
- 1158 Rowan, A., & Pedersen, V. K.: annvrowan/isosia: iSOSIA version used in Schlich-Davies et al. (spm-
 1159 3.3.3r). Zenodo. <https://doi.org/10.5281/zenodo.12666864>, 2024
- 1160 Salerno, F., Guyennon, N., Yang, K., Shaw, T. E., Lin, C., Colombo, N., Romano, E., Gruber, S., Bolch,
 1161 T., Alessandri, A., Cristofanelli, P., Putero, D., Diolaiuti, G., Tartari, G., Verza, G., Thakuri, S.,
 1162 Balsamo, G., Miles, E. S., and Pellicciotti, F.: Local cooling and drying induced by Himalayan
 1163 glaciers under global warming, *Nat. Geosci.*, 16, 1120–1127, <https://doi.org/10.1038/s41561-023-01331-y>, 2023.
- 1165 Sanjay, J., Krishnan, R., Shrestha, A. B., Rajbhandari, R., and Ren, G.-Y.: Downscaled climate change
 1166 projections for the Hindu Kush Himalayan region using CORDEX South Asia regional climate
 1167 models, *Advances in Climate Change Research*, 8, 185–198,
 1168 <https://doi.org/10.1016/j.accre.2017.08.003>, 2017.
- 1169 Sauter, T., Arndt, A., and Schneider, C.: COSIPY v1.3 – an open-source coupled snowpack and ice
 1170 surface energy and mass balance model, *Geosci. Model Dev.*, 13, 5645–5662,
 1171 <https://doi.org/10.5194/gmd-13-5645-2020>, 2020.
- 1172 Shaw, T. E., Miles, E. S., Chen, D., Jouberton, A., Kneib, M., Fugger, S., Ou, T., Lai, H.-W., Fujita, K.,
 1173 Yang, W., Fatichi, S., and Pellicciotti, F.: Multi-decadal monsoon characteristics and glacier
 1174 response in High Mountain Asia, *Environ. Res. Lett.*, 17, 104001, <https://doi.org/10.1088/1748-9326/ac9008>, 2022.
- 1176 Shaw, T. E., Buri, P., McCarthy, M., Miles, E. S., and Pellicciotti, F.: Local Controls on Near-Surface
 1177 Glacier Cooling Under Warm Atmospheric Conditions, *JGR Atmospheres*, 129, e2023JD040214,
 1178 <https://doi.org/10.1029/2023JD040214>, 2024.
- 1179 Shaw, T. E., Miles, E. S., McCarthy, M., Buri, P., Guyennon, N., Salerno, F., Carturan, L., Brock, B.,
 1180 and Pellicciotti, F.: Mountain glaciers recouple to atmospheric warming over the twenty-first
 1181 century, *Nat. Clim. Chang.*, 15, 1212–1218, <https://doi.org/10.1038/s41558-025-02449-0>, 2025.
- 1182 Shea, J. M., Immerzeel, W. W., Wagnon, P., Vincent, C., and Bajracharya, S.: Modelling glacier change
 1183 in the Everest region, Nepal Himalaya, *The Cryosphere*, 9, 1105–1128,
 1184 <https://doi.org/10.5194/tc-9-1105-2015>, 2015.
- 1185 Sherpa, S. F., Wagnon, P., Brun, F., Berthier, E., Vincent, C., Lejeune, Y., et al.: Contrasted surface mass
 1186 balances of debris-free glaciers observed between the southern and the inner parts of the Everest
 1187 region (2007–15). *Journal of Glaciology*, 63(240), 637–651. <https://doi.org/10.1017/jog.2017.30>,
 1188 2017
- 1189 Strickland, R. M., Covington, M. D., Gulley, J. D., Kayastha, R. B., and Blackstock, J. M.: Englacial
 1190 Drainage Drives Positive Feedback Depression Growth on the Debris-Covered Ngozumpa
 1191 Glacier, Nepal, *Geophysical Research Letters*, 50, e2023GL104389,
 1192 <https://doi.org/10.1029/2023GL104389>, 2023.
- 1193 Vacco, D. A., Alley, R. B., and Pollard, D.: Glacial advance and stagnation caused by rock avalanches,
 1194 *Earth and Planetary Science Letters*, 294, 123–130, <https://doi.org/10.1016/j.epsl.2010.03.019>,
 1195 2010.
- 1196 Wagnon, P., Lafaysse, M., Lejeune, Y., Maisincho, L., Rojas, M. and Chazarin, J.P.: Understanding and
 1197 modeling the physical processes that govern the melting of snow cover in a tropical mountain
 1198 environment in Ecuador. *Journal of Geophysical Research: Atmospheres*, 114(D19), 2009.
- 1199 Watson, C. S., Quincey, D. J., Smith, M. W., Carrivick, J. L., Rowan, A. V., and James, M. R.:
 1200 Quantifying ice cliff evolution with multi-temporal point clouds on the debris-covered Khumbu
 1201 Glacier, Nepal, *J. Glaciol.*, 63, 823–837, <https://doi.org/10.1017/jog.2017.47>, 2017.

- 1202 Weidemann, S.S., Sauter, T., Malz, P., Jaña, R., Arigony-Neto, J., Casassa, G. and Schneider, C.: Glacier
1203 Mass Changes of Lake-Terminating Grey and Tyndall Glaciers at the Southern Patagonia Icefield
1204 Derived From Geodetic Observations and Energy and Mass Balance Modeling. *Frontiers in Earth*
1205 *Science*, 6: 81. doi: 10.3389/feart.2018.00081, 2018.
- 1206 Wirbel, A., Jarosch, A. H., and Nicholson, L.: Modelling debris transport within glaciers by advection
1207 in a full-Stokes ice flow model, *The Cryosphere*, 12, 189–204, [https://doi.org/10.5194/tc-12-189-](https://doi.org/10.5194/tc-12-189-2018)
1208 2018, 2018.
- 1209 Zekollari, H., Huss, M., Farinotti, D., and Lhermitte, S.: Ice-Dynamical Glacier Evolution Modeling—
1210 A Review, *Reviews of Geophysics*, 60, <https://doi.org/10.1029/2021RG000754>, 2022.
- 1211
- 1212

1213 **Tables and captions**

1214

1215 Table 1. Regional Climate Models (RCMs) chosen for this study and details of the Global Circulation
 1216 Models (GCMs) from which these are derived.

1217

1218

CORDEX South Asia regional climate model	Driving CMIP5 global climate model	CMIP5 modelling centre	RCM name in this study	Future precipitation scenario (qualitative)	2100 CE mean temperature change from present day (°C)	
					RCP 4.5	RCP 8.5
IITM-RegCM4	NOAA-GFDL-GFDL-ESM2M	National Oceanic and Atmospheric Administration (NOAA), USA	NOAA	Wet	1.4	3.8
IITM-RegCM4	CCCma-CanESM2	Canadian Centre for Climate Modelling and Analysis (CCCma), Canada	CCCma	Moderate	2.2	4.1
IITM-RegCM4	IPSL-CMSA-LR	Institut Pierre-Simon Laplace (IPSL), France	IPSL	Dry	1.6	3.8

1219

1220

1221 Table 2: COSIPY model parameters, where α is albedo (of fresh snow, firn and ice), t^* decay time from
 1222 snow to firn, d^* the constant for the effect of snow depth on albedo, and z_0 surface roughness length.

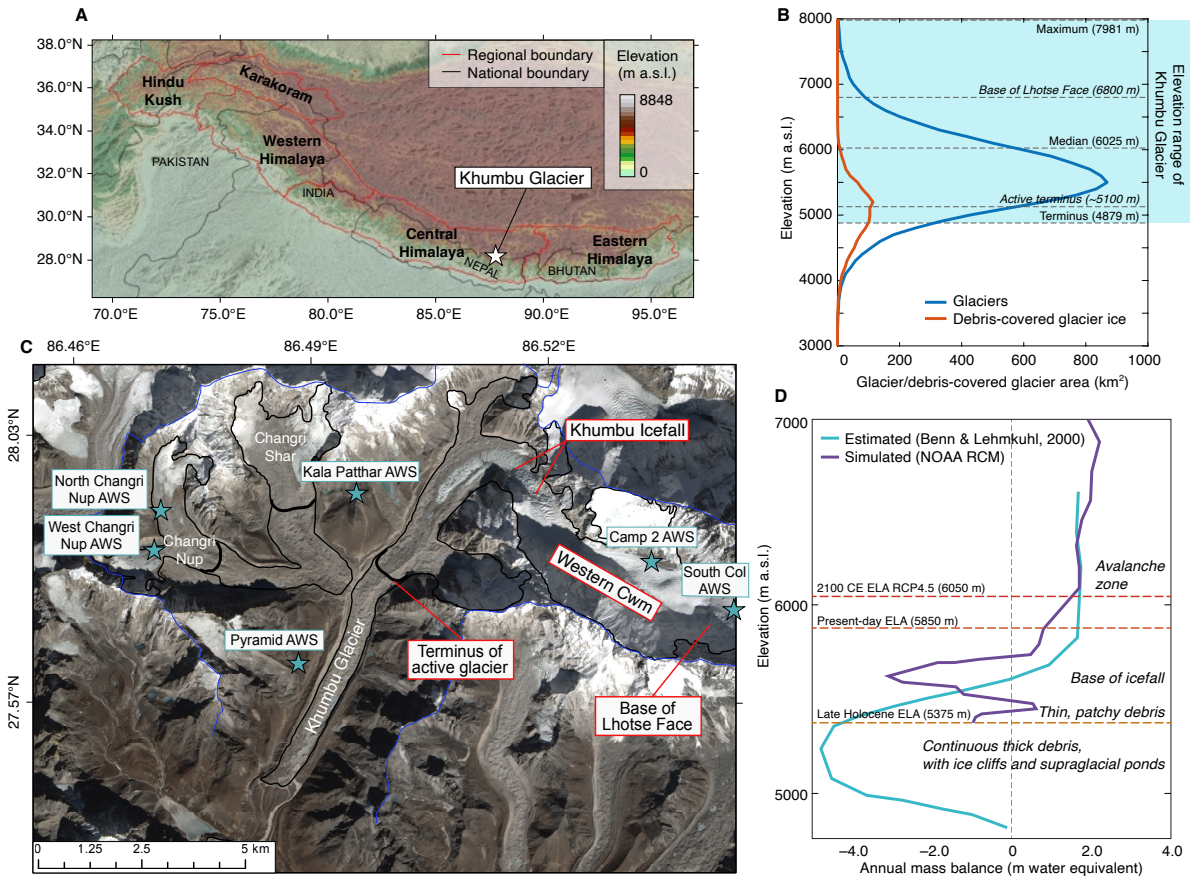
1223

Parameter	Value	Unit	Source
$\alpha_{\text{freshsnow}}$	0.85	-	Mölg et al. 2012; Wagnon et al., 2009
α_{firn}	0.6	-	Knap and Oerlemans, 1996; Mölg et al. 2012
α_{ice}	0.3	-	Mölg et al. 2012
t^*	20	days	Mölg et al. 2012
d^*	1.0	cm	Mölg et al. 2012
$Z_{0\text{snow}}$	0.24	mm	Gromke et al., 2011
$Z_{0\text{firn}}$	4.0	mm	Brock et al., 2006
$Z_{0\text{ice}}$	1.7	mm	Brock et al., 2006
Z_0 ageing length (linearly from $Z_{0\text{snow}}$ to $Z_{0\text{firn}}$)	60	days	Mölg et al. 2012

1224

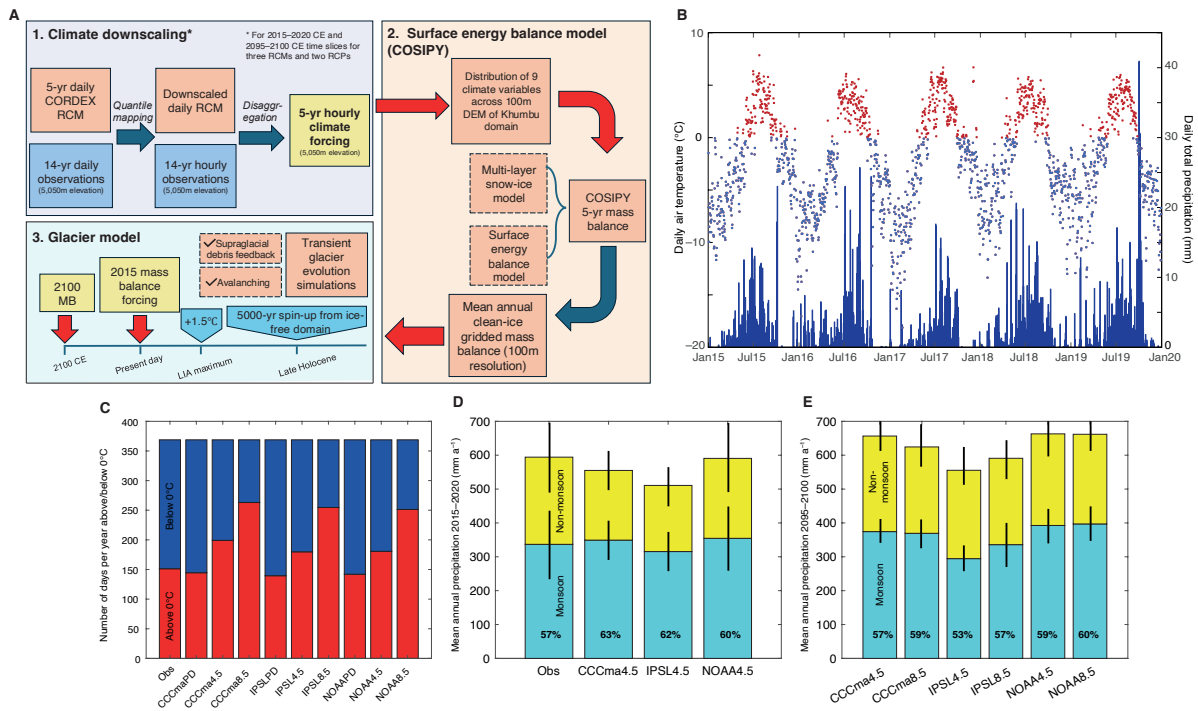
1225
1226

Figures and captions



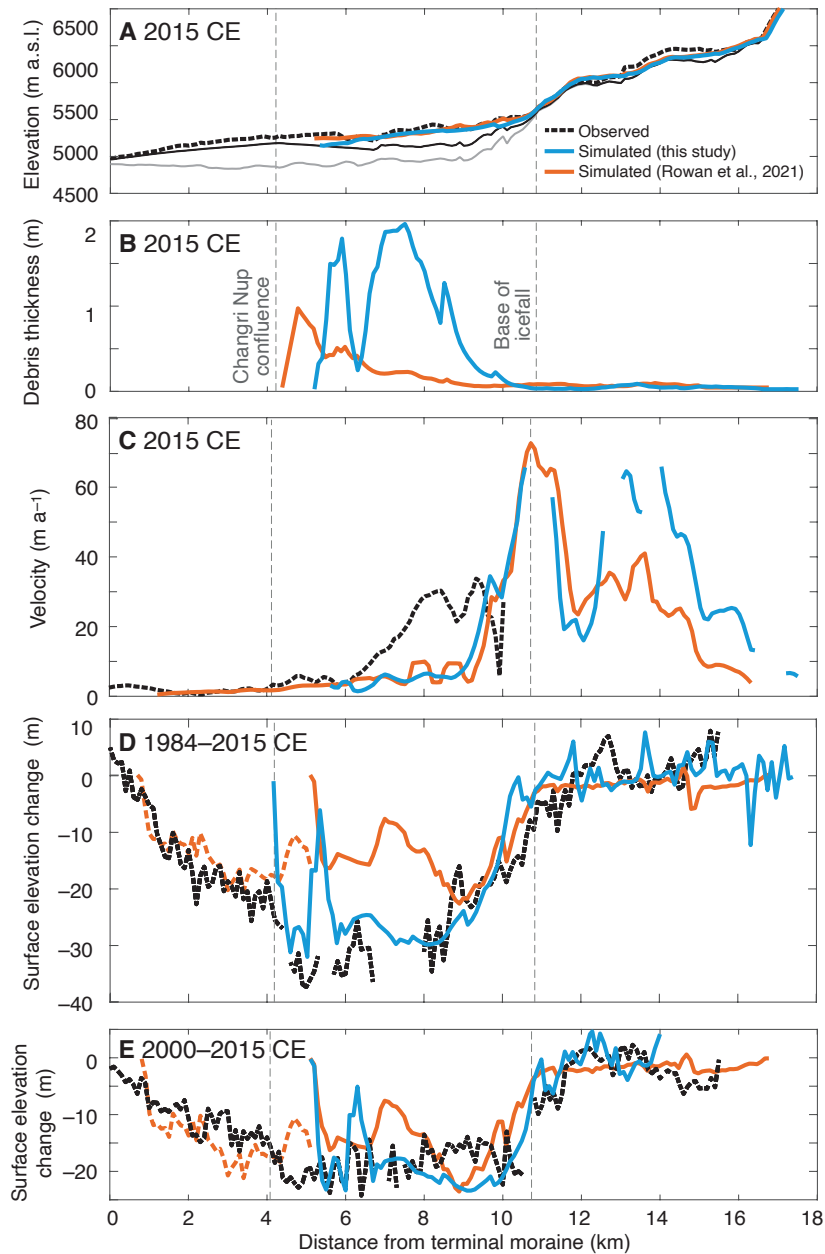
1227
1228
1229
1230
1231
1232
1233
1234
1235
1236
1237
1238
1239
1240
1241
1242
1243
1244

Figure 1: Khumbu Glacier location and context. (a) Map of High Mountain Asia showing the location of the monsoon-influenced Central and Eastern Himalaya and Khumbu Glacier. (b) hypsometry of glaciers and debris-covered glacier ice in the Central and Eastern Himalaya compared with the elevation range of Khumbu Glacier. (c) Map of Khumbu Glacier showing the glacier outline from the RGI database (black line) that is equivalent to the late Holocene (~1 ka) glacier extent identified from ice-marginal moraines, the hydrological catchment that represents the model domain (blue line), the extent of supraglacial debris, location of the Khumbu Icefall, the extent of active ice flow inferred from observations of glacier velocity, and location of the automatic weather stations (AWS) used for RCM downscaling (blue stars). (d) Estimated mass balance gradient for debris-covered glaciers in the Everest region (Benn and Lehmkühl, 2000) compared with the glacier mass balance gradient simulated using the NOAA RCM, and showing change in the equilibrium line altitude (ELA) of Khumbu Glacier in the historical and future simulations for the NOAA RCM RCP4.5 experiment.



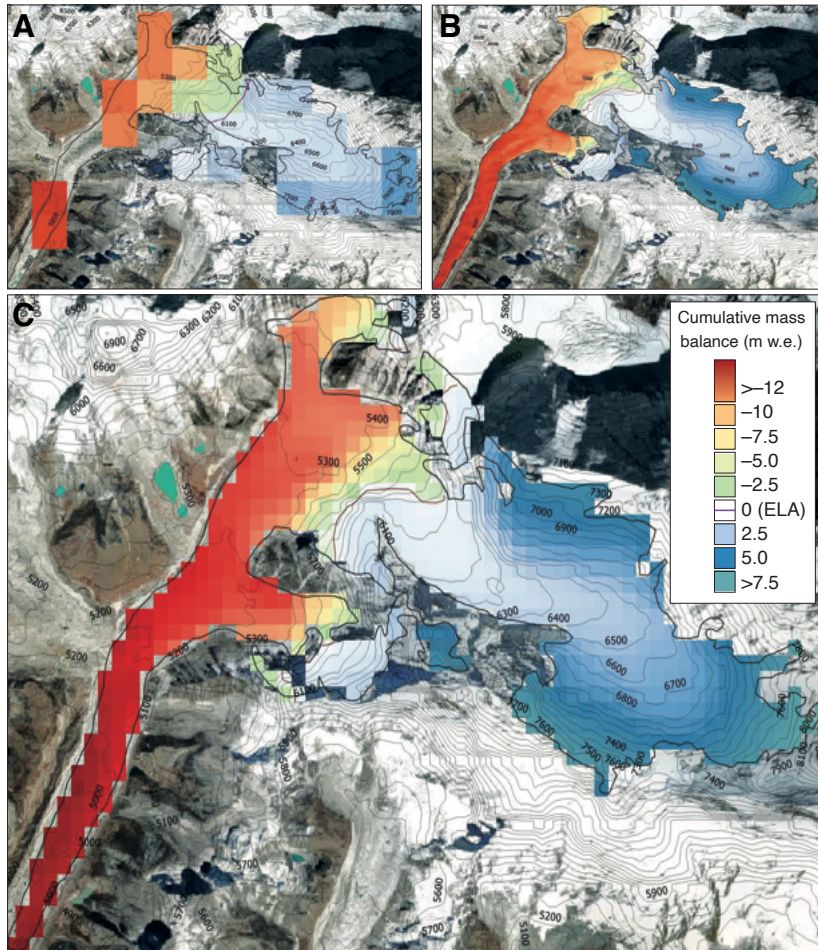
1245
1246
1247
1248
1249
1250
1251
1252
1253
1254
1255
1256
1257
1258
1259
1260
1261
1262
1263
1264
1265
1266

Figure 2: Glacier model experimental design and evaluation of RCM downscaling. (a) Schematic diagram of the glacier modelling approach showing the methods used for downscaling through quantile mapping and disaggregation of climate data. Surface energy balance modelling using COSIPY includes the preprocessing stage of meteorological distribution across the Khumbu domain, which is repeated for each RCM in the 2015–2020 CE climates and for the three RCMs and two RCPs for the 2095–2100 CE climates. The simulated mass balances are then used to force the iSOSIA model. (b) Daily mean temperature and daily total precipitation from the NOAA RCM for the present day (2015–2020 CE) following downscaling using quantile mapping with air temperature categorised into above freezing (red) and below freezing (blue). (c) Proportion of air temperatures above and below freezing for the present day for each RCM and RCP for the downscaled daily data compared with observations. (d) Annual precipitation totals for non-monsoon and monsoon with standard deviation between selected years shown by black bars for the downscaled daily data compared with observations. (e) Future (2095–2100 CE) time-slice annual precipitation totals for non-monsoon and monsoon months with standard deviation between selected years shown by black bars. In (d) and (e) the percentage of the total annual precipitation occurring during the monsoon is indicated by the value in bold text. (Obs = meteorological observations from AWS).



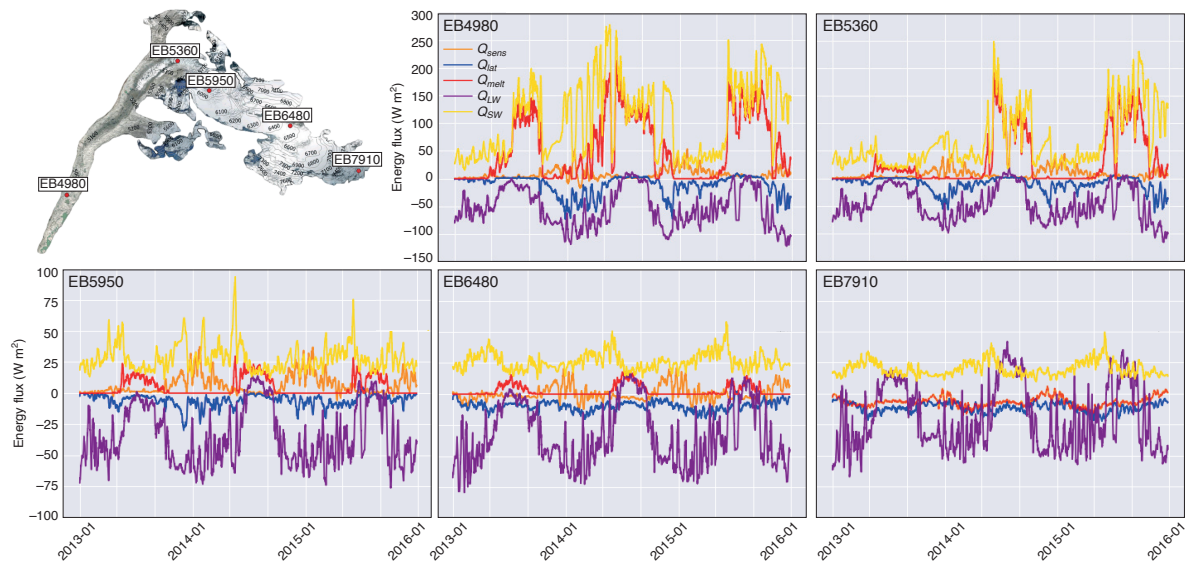
1267
 1268
 1269
 1270
 1271
 1272
 1273
 1274
 1275
 1276
 1277
 1278
 1279
 1280
 1281
 1282
 1283
 1284

Figure 3. Evaluation of NOAA present-day simulation showing; (a) mean simulated glacier surface elevation and bed elevation calculated from a 500 m-wide swath profile along the central flowline of the glacier. Subglacial topography including the dynamically detached debris-covered tongue is shown by the solid black line and subglacial topography used in the entire glacier simulations in Rowan et al. (2015) is shown for comparison by the lowermost grey solid line. The estimated present-day ice surface elevation (Farinotti et al., 2019) is shown by the dashed black line. (b) mean simulated debris thickness, (c) simulated and observed velocities from the NASA MEASUREs ITS_LIVE project (Dehecq et al., 2019), and simulated and observed mean surface elevation change between (d) 1984–2015 CE and (e) 2000–2015 CE using geodetic observations from King et al. (2020) compared with results from the simulations in this study and those in Rowan et al. (2021) where further information about the model evaluation can be found.



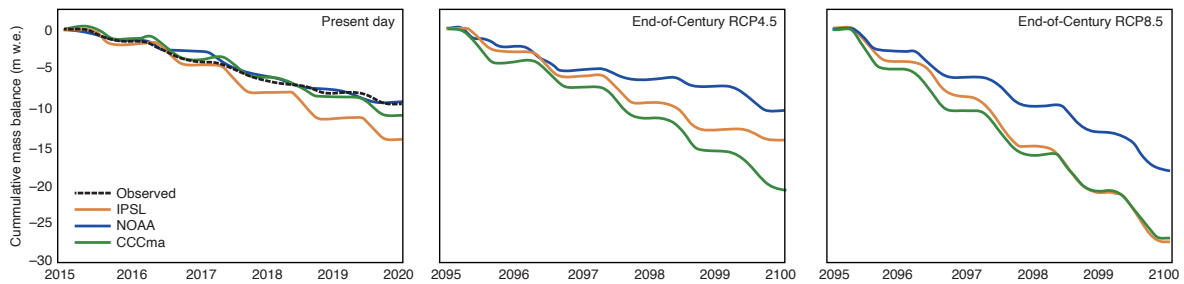
1285
 1286
 1287
 1288
 1289
 1290
 1291
 1292
 1293
 1294
 1295
 1296

Figure 4. COSIPY reference calculation of present-day mass balance for Khumbu Glacier for the period 2013–2015 CE showing the results from calculations using different grid spacings using (a) a 1-km grid, (b) a 30-m grid, (c) the 200-m grid spacing used throughout the experiments in this study.



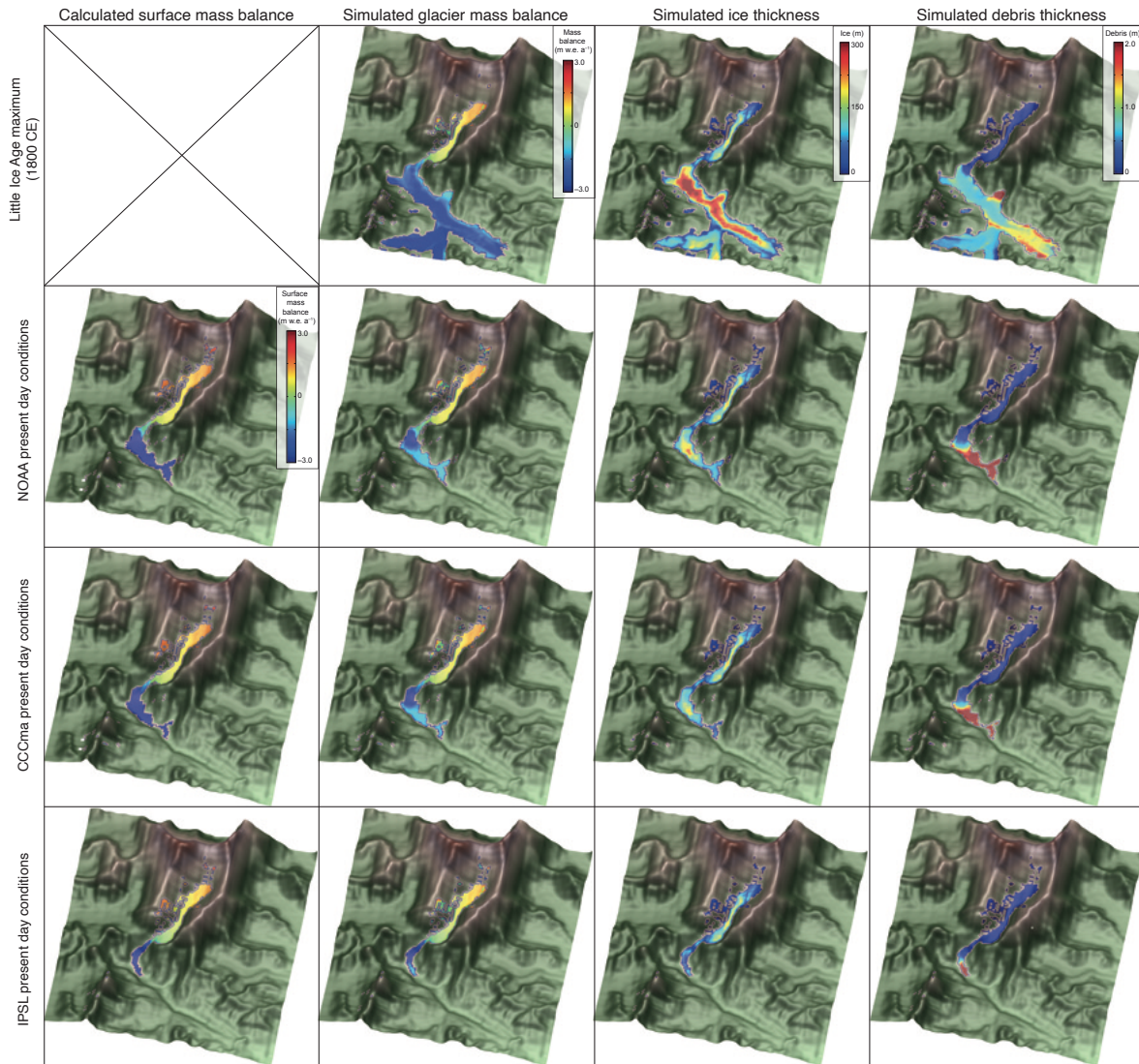
1297
 1298
 1299
 1300
 1301
 1302
 1303
 1304
 1305
 1306
 1307
 1308

Figure 5. Locations of energy balance calculation points used for energy flux and melt components analysis in the reference calculation and sensitivity tests (named after their corresponding altitude e.g., EB6480) showing 5-day average of energy fluxes across study period for each site. Note that scales for energy flux are different for the two sites below the icefall compared to the three sites above the icefall.



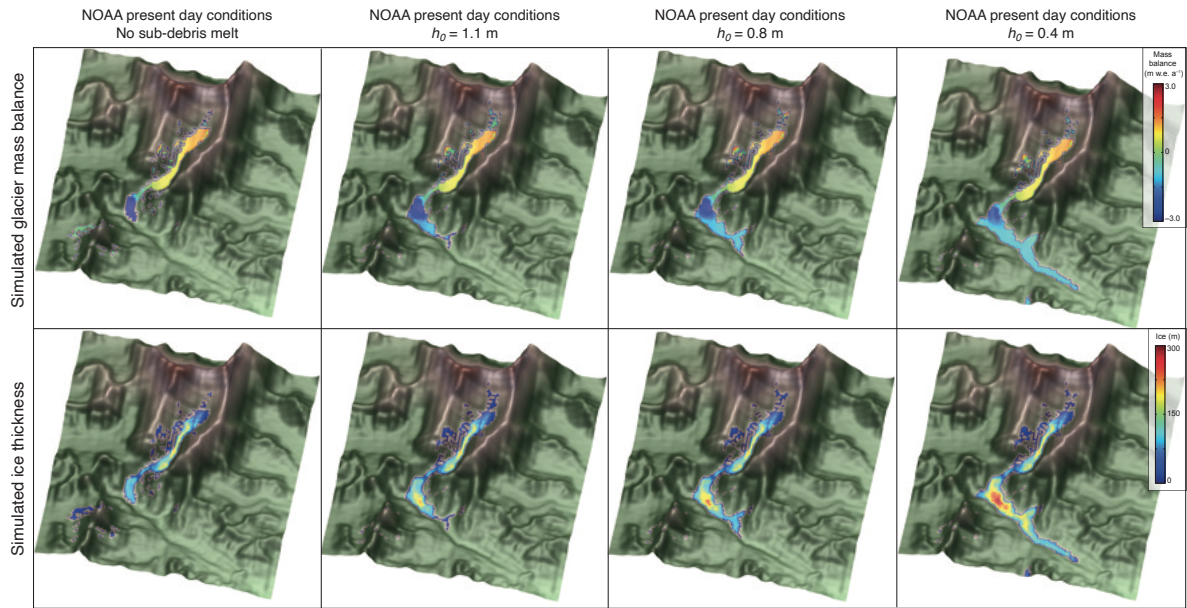
1309
 1310
 1311
 1312
 1313
 1314
 1315
 1316
 1317
 1318
 1319

Figure 6. Spatially averaged cumulative clean-ice mass balance with clear seasonality for the present day time slice including the mass balance forced by the observations used for downscaling, and the end-of-Century time slice under RCP4.5 and RCP8.5. The low annual glacier-wide mass balance values shown here result from the extent of the model domain used to force the glacier model that includes the larger catchment beyond the glacier margins and therefore contains a higher proportion of lower elevations than those of the glacier itself. However the similarity between the mass balance results for simulations forced by NOAA RCM and observations can be clearly seen, and the differences between the three RCMs is apparent in all time slices.



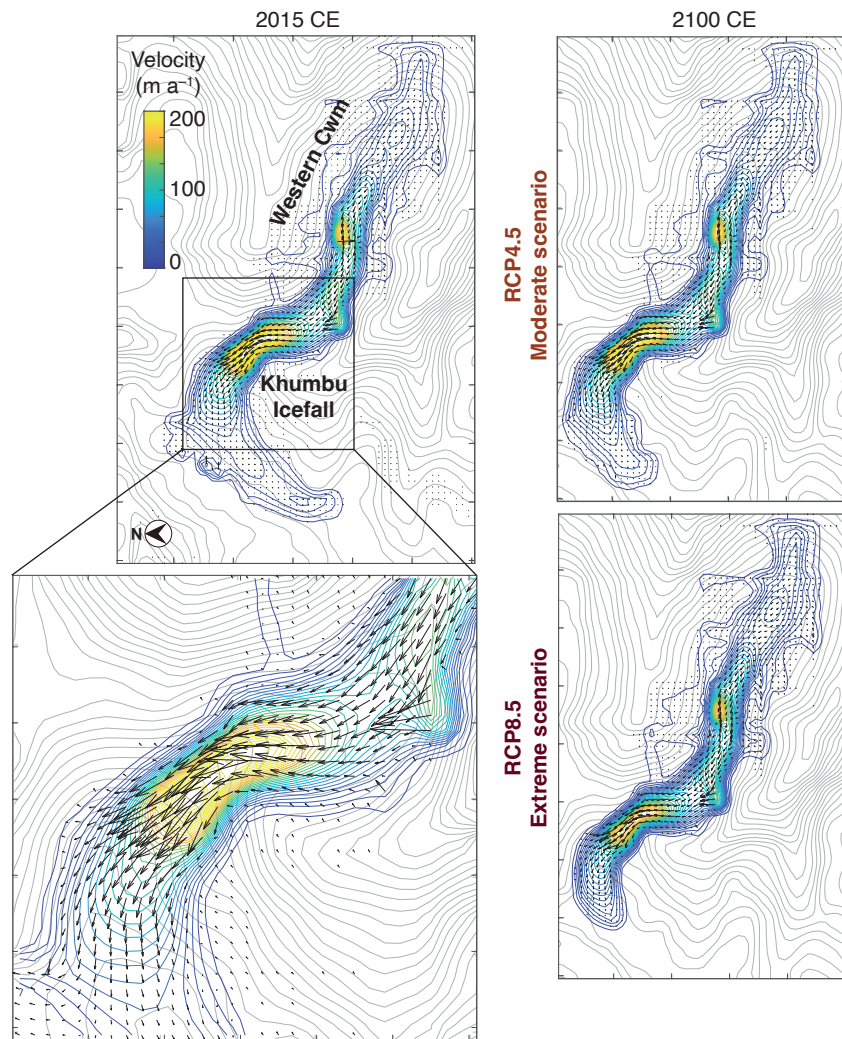
1320
 1321
 1322
 1323
 1324
 1325
 1326
 1327
 1328

Figure 7. iSOSIA model sensitivity to surface energy and mass balance forcing, showing ‘Little Ice Age’ (~1800 CE) maximum glacier mass balance, ice thickness and debris thickness. Present-day results for surface mass balance calculated using each RCM with COSIPY showing glacier mass balance calculated using the same climate forcing following integration with the glacier model, simulated ice thickness, and simulated debris thickness.



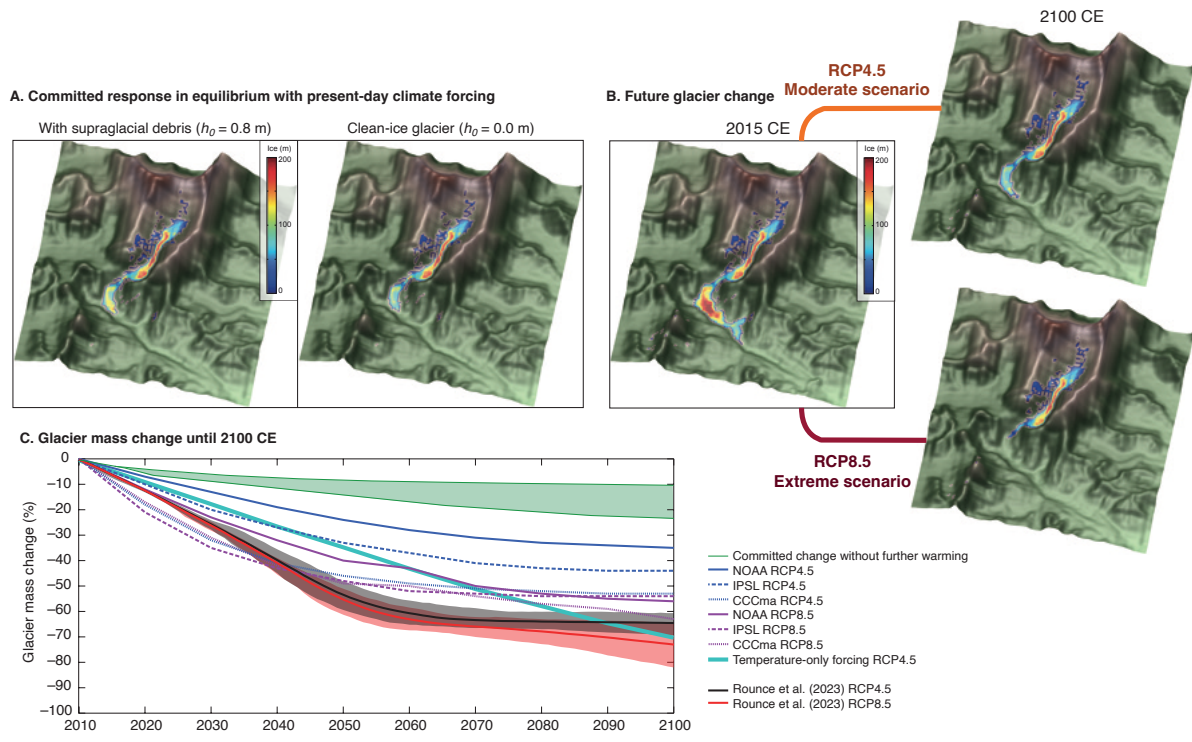
1329
 1330
 1331
 1332
 1333
 1334
 1335
 1336
 1337
 1338
 1339

Figure 8. Glacier mass balance and ice thickness simulated using the NOAA RCM climate forcing and the resulting simulated ice thickness where no sub-debris melt is imposed and the glacier has an entirely debris-free surface compared with ice results for simulations with h_0 values of 0.4 m, 0.8 m, and 1.1 m where h_0 is a constant in Equation (1) representing the characteristic debris thickness at which the reduction in ablation due to insulation by supraglacial debris is 50% of the value for an equivalent clean-ice surface (Anderson and Anderson, 2016; Rowan et al., 2021) .



1340
 1341
 1342
 1343
 1344
 1345
 1346
 1347
 1348
 1349
 1350
 1351

Figure 9. Simulated ice flow for Khumbu Glacier. Velocity-vector maps showing simulated ice flow magnitude and direction from the present day (2015–2020 CE) and 2100 CE under RCP4.5 and RCP8.5 using the downscaled NOAA climate forcing. Simulated ice flow speed is shown as colour shading with blue contours, and the bed topography is shown by grey contours. The outermost contour in each plot represents the slowest ice flow close to the glacier margins with depth-integrated velocities of 5–10 m a⁻¹. Note that rapid flow across the Western Cwm indicated by a single arrow represents the effects of avalanching rather than sustained glacier flow.



1352
 1353
 1354
 1355
 1356
 1357
 1358
 1359
 1360
 1361
 1362
 1363
 1364
 1365

Figure 10. Future glacier volume change projections until 2100 CE. (a) Equilibrium ice thickness accounting for the committed response to recent climate change using the downscaled NOAA RCM climate forcing with and without the effect of supraglacial debris on mass balance. (b) Simulated ice thickness under RCP4.5 and RCP8.5 for 2100 CE using the downscaled NOAA RCM climate forcing. (c) Comparison of projected shrinkage of Khumbu Glacier by 2100 CE from this study with those from Rounce et al. (2023) showing results from each of the six experiments in this study with results from RCP4.5 and RCP8.5 from Rounce et al. (2023), the equivalent result for a simulation using a change in MAAT equivalent to the NOAA RCP4.5 forcing where precipitation does not change from the present-day value (cyan line). The green shading shows the range of the committed volume loss due to historical warming.

1366 **Appendix**

1367 This appendix contains further details on the meteorological data collection and analysis, RCM
1368 downscaling, evaluation of the present-day downscaled RCM results using meteorological data and the
1369 distribution of these results across the model domain, and the parameterisation and sensitivity testing
1370 of the COSIPY model. The Indian Summer Monsoon season was defined as June to October, the post-
1371 monsoon as October–November, winter as December–February, and the pre-monsoon as March–May
1372 (Ueno et al., 2008). Although much of this study compares the monsoon season against the non-
1373 monsoon season, it should be noted that the timing of monsoon onset and cessation can vary between
1374 years. Day time was defined as 08:00–16:00 and night as 20:00–04:00 (Nepal local time) to account for
1375 changing sunrise and sunset times throughout the year and the influence of topographic shading in the
1376 valleys; centred-means were used for some datasets to remove local noise associated with daily
1377 frequencies. For sub-hourly measurements, hourly averages were calculated using data from the
1378 previous hour. The period for the reference simulation and sensitivity experiments was January 1st 2013
1379 to December 31st 2015. RCM downscaling to produce the five-year time slices represented the periods
1380 January 1st 2015 to December 31st 2019 and January 1st 2095 to December 31st 2099.

1381

1382 **A1. Gap filling of the AWS data**

1383 All AWS datasets contained periods of erroneous measurements and missing data, which is unsurprising
1384 given the challenges of maintaining equipment in such an environment (Oulkar et al., 2026). Daily air
1385 temperature averages were calculated when 83% (20 hours) of observations were available. For
1386 calculation of lapse rates for longer time periods (e.g. daytimes during the monsoon season) the
1387 distributions of missing data across these periods were analysed. For example, the Lukla AWS had
1388 almost 45% of temperature observations missing during the monsoon season but as these were equally
1389 distributed between day and night, lapse rates could be calculated using station pairs following the
1390 method of Immerzeel et al. (2014). Up to 13% of the West Changri Nup AWS temperature records were
1391 missing, and these were interpolated using the Ev-K2-CNR Pyramid AWS data with the same lapse rate
1392 as the GlacioClim dataset. The interpolated results were compared with the preceding and succeeding
1393 periods from the same AWS, and the preceding and succeeding months from other AWS, and compared
1394 with data collected in November 2014 at the GlacioClim North Changri Nup AWS (5,470 m a.s.l.).

1395

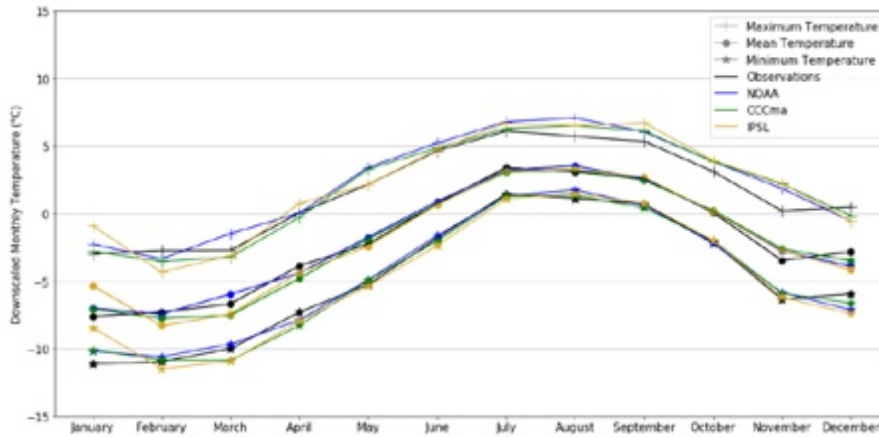
1396 Data gaps in the precipitation datasets were significant, particularly during the onset of the monsoon
1397 (e.g., 45% of data points were missing for the Namche AWS) meaning the altitudinal dependency of
1398 precipitation could not be fully characterised. This led to several monsoon seasons with little or no data
1399 at individual AWS. Given that the aim of this study was to analyse *in situ* trends, gap-filling through
1400 interpolation was not conducted for these AWS during the seasons without data. Station pairs were used
1401 to determine the elevation dependency of precipitation for the reference simulation following the
1402 method of Immerzeel et al. (2014). Results from the Kala Patthar/Pheriche station pair and the
1403 Pyramid/Pheriche station pair in 2009, and the Kala Patthar/Namche station pair during 2011, show that
1404 the relationship between precipitation amount and elevation was more negative during the monsoon
1405 season ($-0.011\% \text{ m}^{-1}$ to $-0.018\% \text{ m}^{-1}$) than during the non-monsoon ($-0.0039\% \text{ m}^{-1}$ to $-0.0043\% \text{ m}^{-1}$).
1406 No interpolation to fill data gaps was required for other meteorological variables, apart from albedo
1407 but as this was only measured at the West Changri Nup AWS there was no suitable surrogate for this
1408 variable.

1409

1410 **A2. Downscaled climate model results compared with observations**

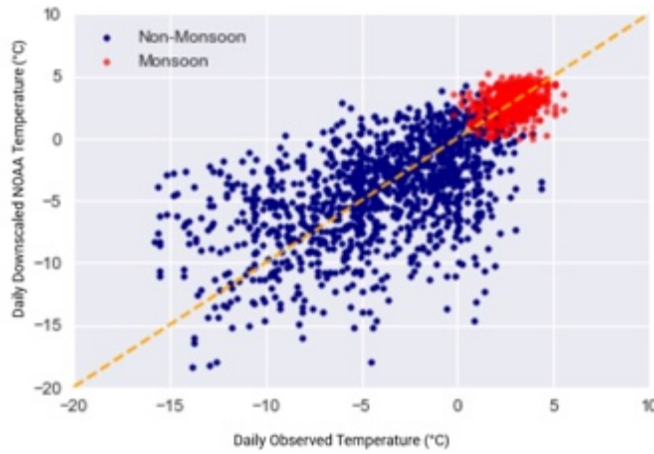
1411

1412



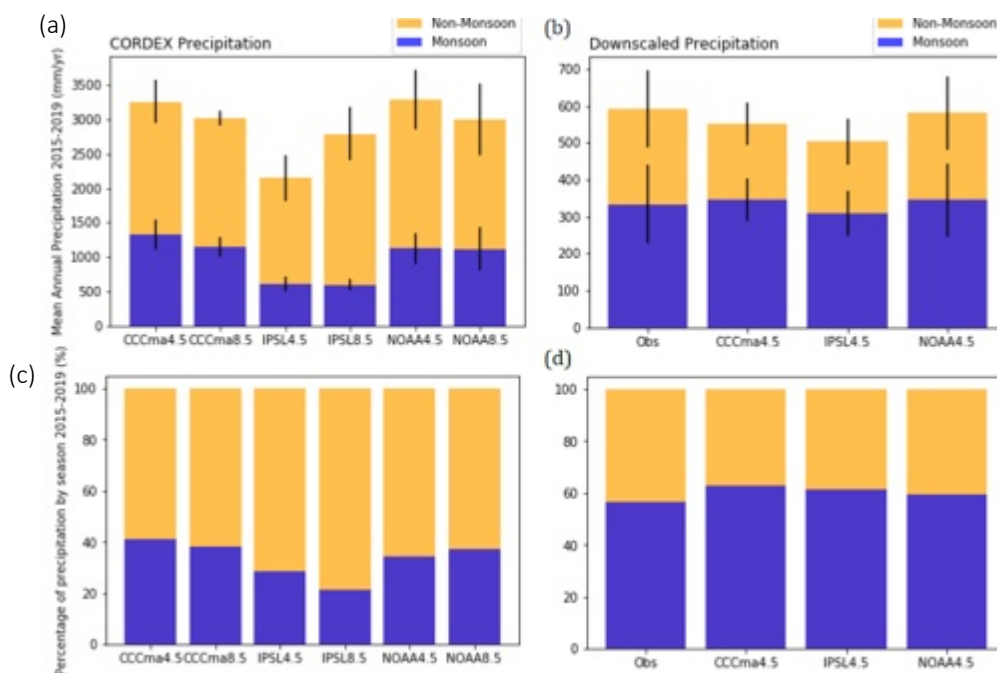
1413
 1414
 1415
 1416
 1417
 1418
 1419
 1420
 1421

Figure A1: Downscaled monthly mean, maximum, and minimum temperature calculated for the present day time slice compared with observations from the GlacioClim Pyramid Observatory AWS.



1422
 1423
 1424
 1425
 1426
 1427
 1428
 1429
 1430

Figure A2: Daily downscaled temperature from the NOAA RCM against observations from the GlacioClim Pyramid Observatory AWS split by monsoon/non-monsoon. The 1:1 relationship is shown by the dashed orange line.

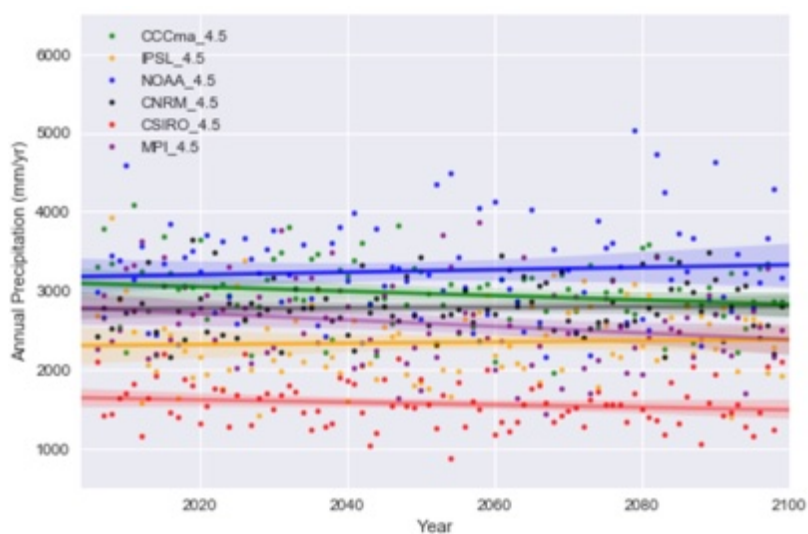


1431
 1432
 1433
 1434
 1435
 1436
 1437
 1438
 1439
 1440
 1441
 1442
 1443
 1444
 1445
 1446

Figure A3. Annual precipitation totals for the monsoon and non-monsoon seasons. (a and b) Precipitation totals before and after downscaling, with the standard deviation between selected years shown by black bars. (c and d) The same results as seasonal percentages. The annual precipitation is in good agreement with measurements in the southern Dudh Koshi catchment for the gridbox nearest to Khumbu Glacier is located at 27.9065056°N, 86.4352951°E at 2,100 m a.s.l..

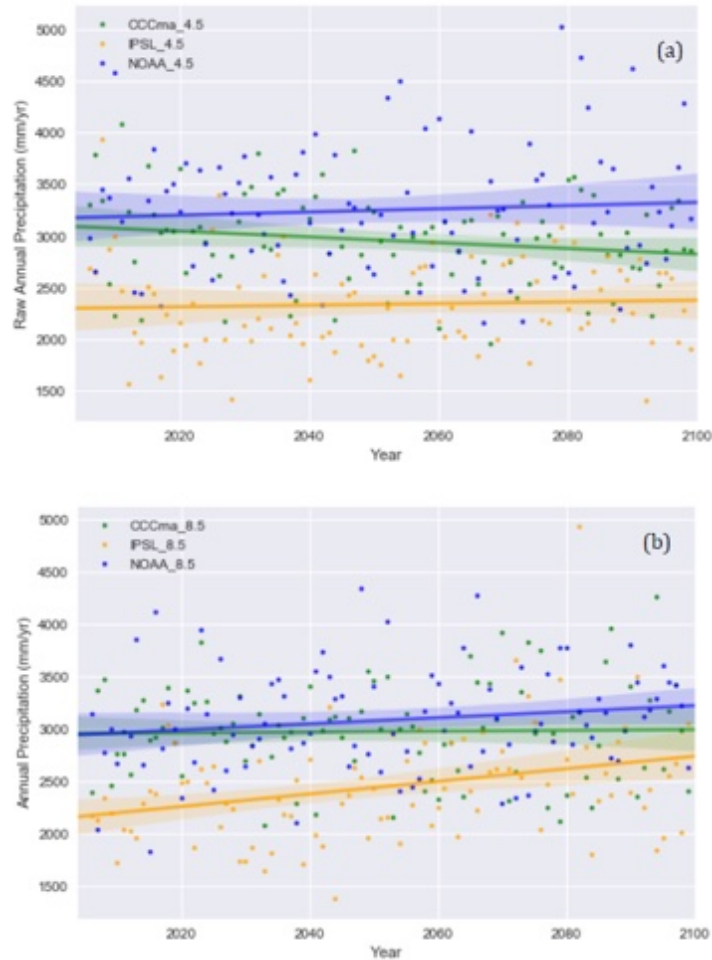
A3. Regional Climate Model analysis and selection

Three of the six available CORDEX South Asia RCMs (NOAA, CCCma, IPSL) were selected as discrete scenarios that spanned the range of possible future precipitation conditions (Table 1); either wet, moderate, or dry climate in 2080–2100 CE (Fig. A4). The raw RCMs significantly overestimated the annual total precipitation by at least a factor of five for the selected gridpoint, which was corrected by downscaling of these results using the AWS data.



1447
 1448
 1449
 1450
 1451

Figure A4: Annual precipitation sums (dots) with fitted trend line from the start of the RCP experiments (2006–2100 CE) for each of the six Indian Institute for Tropical Meteorology CORDEX models for RCP4.5.



1452
 1453
 1454
 1455
 1456
 1457
 1458
 1459
 1460
 1461
 1462
 1463
 1464
 1465
 1466
 1467
 1468

Figure A5: Annual precipitation sums (dots) with fitted trend line from the start of the RCP experiments (2006–2100 CE) for the three selected of the six CORDEX models for (a) RCP4.5 and (b) RCP8.5.

A4. Downscaling parameters and method

While minimum and maximum air temperatures are not required to as inputs to COSIPY, these were downloaded and statistically downscaled using quantile mapping with normal distribution to aid disaggregation to an hourly time step using MELODIST (Table A1). Quantile mapping for the CORDEX wind speed data was found to be ineffective when analysing the time series output against observations, both for the absolute wind speed as well as the reduced day-on-day variability seen during the monsoon season, and therefore, GARD was used instead. This is a simple statistical analogue regression downscaling method appropriate for pointwise downscaling.

Table A1: RCM-derived parameters and the method used for downscaling or bias correction.

RCM-derived parameters	Downscaling/bias correction method	Parametric distribution model (for Quantile mapping)	References
Precipitation (kg per m ² per s, converted to mm day ⁻¹)	Quantile mapping	Gamma	Vrac et al., 2007; Piani et al., 2010
Mean temperature (K) Minimum temperature (K) Maximum temperature (K)	Quantile mapping	Normal / Gaussian	Li et al., 2010, Gupta et al., 2016; Luo et al., 2018
Incoming shortwave (W m ⁻²) Incoming longwave (W m ⁻²)	Quantile mapping	Beta	Ruane et al., 2015

Relative humidity (%)			
Pressure (hPa)	Bias correction	N/A	N/A
Wind speed (m s ⁻¹)	Regression downscaling	N/A	Gutmann et al., 2022

1469

1470

1471

A5. Variability in surface energy balance with elevation

1472

1473

1474

1475

1476

1477

1478

1479

1480

1481

1482

1483

correlated exactly with the sensible heat flux.

1484

1485

1486

1487

1488

1489

1490

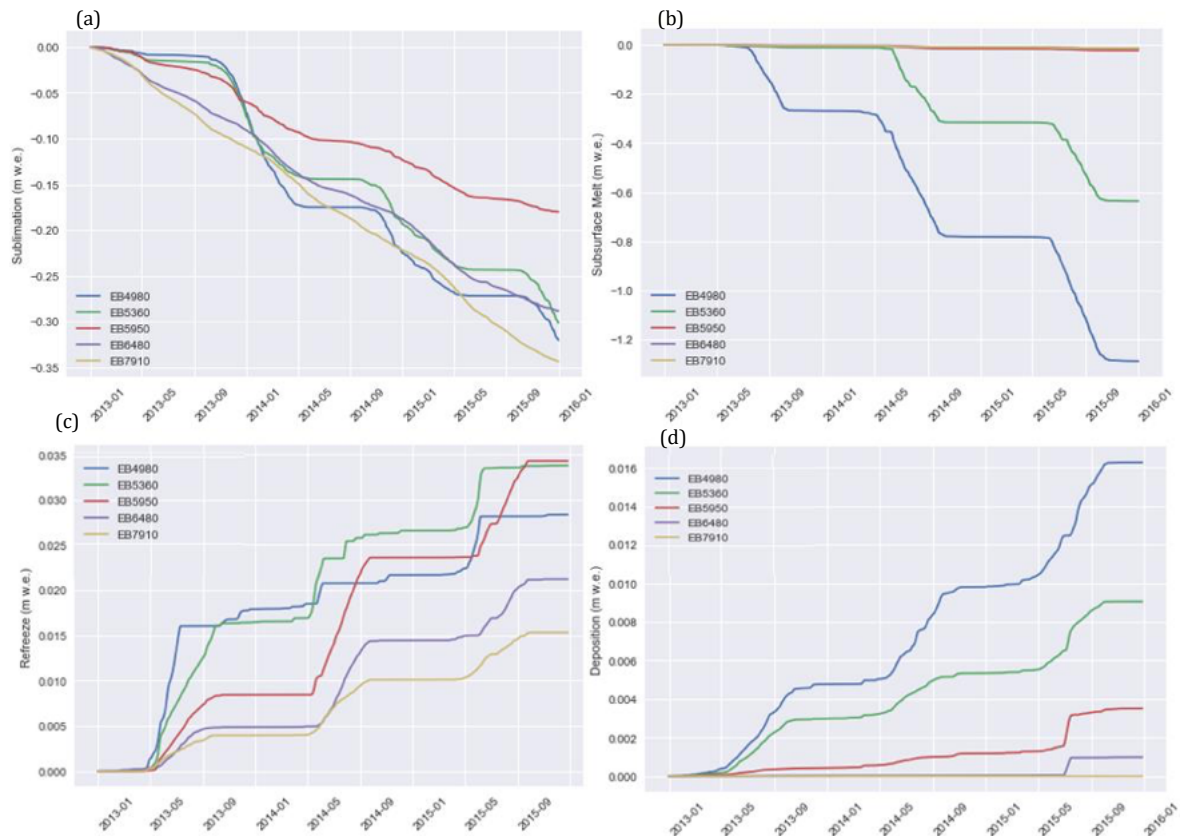
1491

1492

1493

1494

Sublimation occurred at all elevations, with the highest cumulative loss at EB7910 (Fig. A6A). Sublimation rates correlated with seasonality down-glacier; at EB7910 sublimation only slightly slowed from December until May, while sublimation at site EB4980 increased from April until the start of the monsoon in July. Subsurface melt at or above the ELA (5,950 m a.s.l.) was negligible, but lower elevation sites showed stronger seasonal cycles related to surface temperatures. Refreezing (Fig. A6C) occurred at all sites and the onset of refreezing was staggered with increasing elevation, although absolute values remained low. Higher Q_{lat} during the monsoon resulted in higher deposition of snow to the glacier at lower elevations and negligible rates at higher elevations. Similar absolute values and patterns are seen for condensation (results not shown).



1495
1496
1497
1498
1499
1500
1501

Figure A6. 5-day averages of (a) sublimation, (b) subsurface melt, (c) refreeze, and (d) deposition for the five surface energy balance sensitivity testing sites across Khumbu Glacier (see Fig. 5 for locations of these sites).

A6. COSIPY parameter testing and sensitivity results

1502 To isolate the impact of individual surface energy balance variables on the mass balance of Khumbu
1503 Glacier, each variable was perturbed individually, and air temperature and precipitation amount were
1504 tested in tandem for the reference period 2013–2015 CE (Table A2). Perturbations of all variables were
1505 within the range of possible uncertainty that arise from a combination of observations, climate models,
1506 downscaling approach or the distribution of meteorology. The positive temperature and precipitation
1507 perturbations were in the order of possible future climate forcings. The spatially averaged mass balance
1508 was most sensitive to changes in LW_{in} , air temperature, and SW_{in} , and relative humidity had the least
1509 impact on ablation/accumulation rates (Fig. A7). The coupled parameter testing (Fig. A8) perturbed
1510 precipitation and air temperature simultaneously. The most significant change in spatially averaged
1511 mass balance followed a 3°C increase in air temperature and 20% decrease in precipitation amount. The
1512 increase in ablation following an increase in air temperature of 1.5°C was completely compensated by
1513 the increase in accumulation resulting from a 20% increase in precipitation amount.

1514
1515
1516 Accurate estimation of precipitation phase is important for summer-accumulation type glaciers and
1517 threshold values of air temperature are often used to separate liquid and solid precipitation. Previous
1518 work calculated threshold temperatures across 6,883 AWS in the Northern Hemisphere to find an
1519 average rain/snow partitioning value of 1°C, with 95% of observations falling between 0.4°C and 2.4°C
1520 (Jennings et al., 2018). Although there remains a lack of such data for High Mountain Asia, Jennings et
1521 al. (2018) found that high mountain areas have the highest rain/snow partitioning thresholds, with a
1522 value of up to 4.5°C on the Tibetan Plateau. The impact of two different precipitation partitioning
1523 schemes on glacier mass balance was investigated here. Threshold temperatures of 0.5°C, 2.0°C and

1524 3.5°C were chosen and compared with the default value in COSIPY (STF), and a scheme that smoothly
 1525 scaled from 100% solid precipitation at -1°C to 0% solid precipitation at 4°C was also tested.

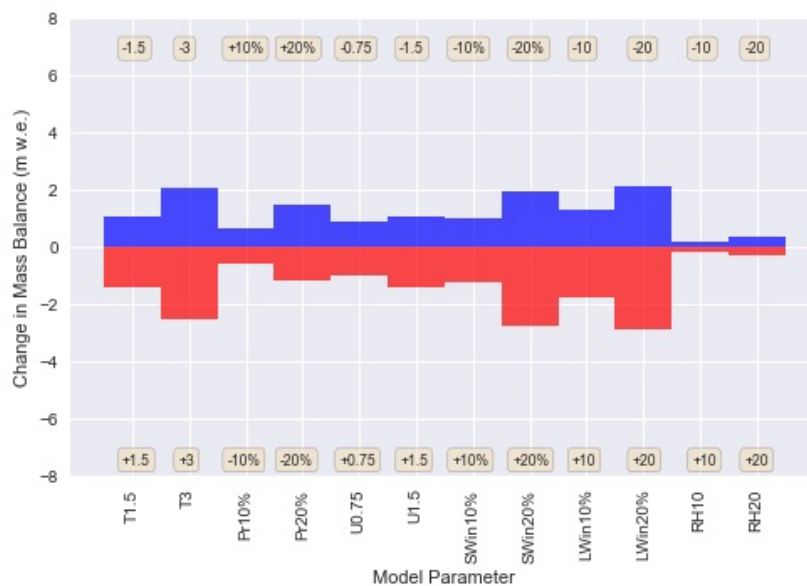
1526
 1527 The glacier ice surface roughness (z_0) was defined as 1.7 mm for the reference simulation, which is a
 1528 reasonable estimate for clean-ice glaciers (Mölg et al., 2012). The z_0 values reported within the literature
 1529 vary widely for clean-ice glaciers, and two substantially different z_0 values were tested. A z_0 value of
 1530 0.1 mm was measured at Midtre Lovénbreen, Svalbard (Irvine-Fynn et al. 2014), and August-One
 1531 glacier, China (Guo et al., 2018), and a z_0 value of 6.9 mm was calculated on the clean-ice section of
 1532 the Haut Glacier D’Arolla (Brock et al., 2006) and Laohugou Glacier No. 12 (Sun et al., 2018). These
 1533 values were used as endmembers of the likely range in values for Khumbu Glacier. The z_0 value had
 1534 minimal impact on glacier mass balance (Fig. A9) although a higher (lower) value for z_0 did result in
 1535 slightly increased (decreased) mass balance. The mass balance sensitivity was not proportional to the
 1536 change in z_0 , with a z_0 value of 1.6 mm lower than the reference value leading to a similar mass balance
 1537 change than that of the experiment with a z_0 value of 5.2 mm higher than the reference value.

1538
 1539 The albedo values of the three glacier components were perturbed by ± 0.05 from that used in the
 1540 reference experiment (e.g., 0.85 for fresh snow). There was a strong response of the glacier mass balance
 1541 to changing snow albedo. Reducing snow albedo by 0.05 led to a 65% reduction in mass balance of
 1542 2.21 m w.e. (Fig. A9). Ablation (accumulation) rates were 3.7 m w.e. (1.75 m w.e.) higher relative to
 1543 the reference simulation for this perturbation. This result further supports the importance of Q_{SW} to
 1544 ablation rates. Varying albedo values for firn and ice also revealed a lower sensitivity of glacier mass
 1545 balance relative to snow albedo.

1546
 1547
 1548 Table A2. Parameter perturbations for the sensitivity experiments. Note that for relative humidity the %
 1549 refers to the units and not the perturbation.

Parameter	Perturbation
Mean annual air temperature (C)	$\pm 1.5, \pm 2.0, \pm 3.0$
Precipitation amount (%)	$\pm 10, \pm 20, \pm 30$
Wind speed ($m s^{-1}$)	$\pm 0.75, \pm 1.5$
SW_{in} and LW_{in} (%)	$\pm 10, \pm 20$
Relative Humidity (%)	$\pm 10, \pm 20$

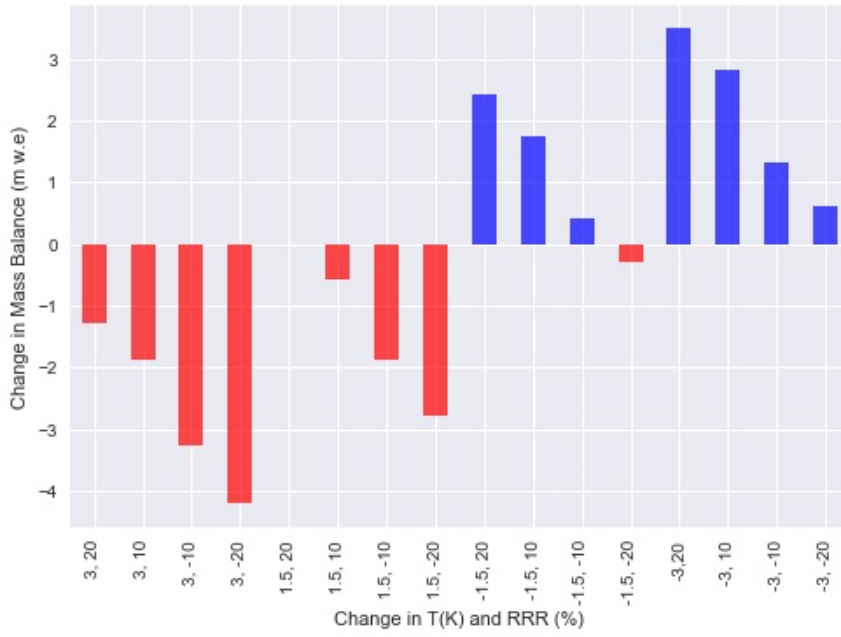
1551



1552

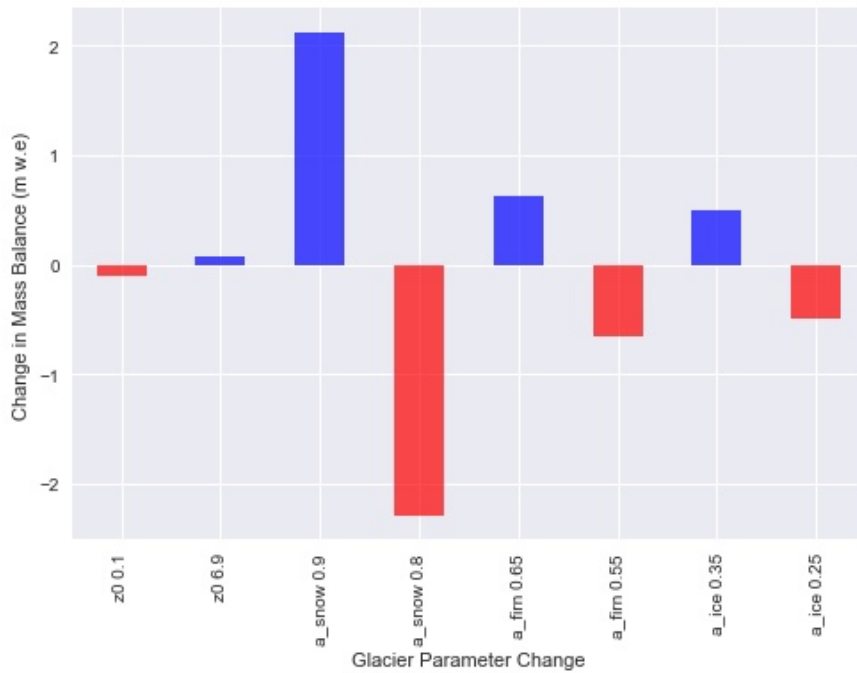
1553

1554 Figure A7. Single parameter sensitivity test results for reference simulation period 2013–2015 CE.



1555
 1556
 1557
 1558
 1559
 1560
 1561

Figure A8. Coupled parameter sensitivity test results for mean annual air temperature and precipitation amount for reference simulation period 2013–2015 CE.



1562
 1563
 1564
 1565
 1566
 1567
 1568
 1569
 1570
 1571

Figure A9. Sensitivity of mass balance for the reference simulation period 2013–2015 CE to changing glacier parameters (surface roughness, and albedo of snow, firm, and ice).

1572 **Additional references for Appendix A**

- 1573 Gupta, A. and Tarboton, D.G.: A tool for downscaling weather data from large-grid reanalysis products
1574 to finer spatial scales for distributed hydrological applications. *Environmental Modelling &*
1575 *Software*. 84, pp. 50–69. <https://doi.org/10.1016/j.envsoft.2016.06.014>, 2016
- 1576 Gutmann, E. D., J. J. Hamman, M. P. Clark, T. Eidhammer, A. W. Wood, and J. R. Arnold: En-GARD:
1577 A Statistical Downscaling Framework to Produce and Test Large Ensembles of Climate
1578 Projections. *J. Hydrometeor.*, 23, 13545–1561, <https://doi.org/10.1175/JHM-D-21-0142.1>, 2022
- 1579 Immerzeel, W., Petersen, L., Ragetti, S. and Pellicciotti, F.: The importance of observed gradients of
1580 air temperature and precipitation for modelling runoff from a glacierized watershed in the
1581 Nepalese Himalayas. *Water Resources Research*. 50: 2212-2226. doi: 10.1002/2013WR014506,
1582 2013
- 1583 Jennings, K. S., Winchell, T. S., Livneh, B., and Molotch, N. P.: Spatial variation of the rain–snow
1584 temperature threshold across the Northern Hemisphere, *Nat Commun*, 9, 1148,
1585 <https://doi.org/10.1038/s41467-018-03629-7>, 2018.
- 1586 Lente, G. and Ósz, K.: Barometric formulas: various derivations and comparisons to environmentally
1587 relevant observations. *ChemTexts*, 6, pp.1-14. <https://doi.org/10.1007/s40828-020-0111-6>, 2020
- 1588 Li, H., Sheffield, J. and Wood, E.F.: Bias correction of monthly precipitation and temperature fields
1589 from Intergovernmental Panel on Climate Change AR4 models using equidistant quantile
1590 matching. *Journal of Geophysical Research: Atmospheres*, 115(D10).
1591 <https://doi.org/10.1029/2009JD012882>, 2010
- 1592 Oulkar, S. N., Peacey, M. W., Mitrev, M., Quincey, D. J., Hubbard, B., Matthews, T., Oulkar, A. S.,
1593 Miles, K. E., and Rowan, A. V.: Design and implementation of a robust data logging and satellite
1594 telemetry system for remote cryospheric research, *Geosci. Instrum. Method. Data Syst.*, 15, 75–
1595 88, <https://doi.org/10.5194/gi-15-75-2026>, 2026.
- 1596 Ruane, A. C., Goldberg, R., and Chryssanthacopoulos, J.: Climate forcing datasets for agricultural
1597 modeling: Merged products for gap-filling and historical climate series estimation, *Agricultural*
1598 *and Forest Meteorology*, 200, pp. 233–248. <https://doi.org/10.1016/j.agrformet.2014.09.016>,
1599 2015
- 1600 Salerno, F., Guyennon, N., Thakuri, S., Viviano, G., Romano, E., Vuillermoz, E., Cristofanelli, P.,
1601 Stocchi, P., Agrillo, G., Ma, Y., and Tartari, G.: Weak precipitation, warm winters and springs
1602 impact glaciers of south slopes of Mt. Everest (central Himalaya) in the last 2 decades (1994–
1603 2013), *The Cryosphere*. 9: 1229-1247. doi: 10.5194/tc-9-1229-2015, 2015
- 1604 Sun, W., Qin, X., Wang, Y. et al. The response of surface mass and energy balance of a continental
1605 glacier to climate variability, western Qilian Mountains, China. *Clim Dyn* 50, 3557–3570,
1606 <https://doi.org/10.1007/s00382-017-3823-6>, 2018
- 1607 Vrac, M., Stein, M.L., Hayhoe, K. and Liang, X.Z.: A general method for validating statistical
1608 downscaling methods under future climate change. *Geophysical Research Letters*, 34(18).
1609 <https://doi.org/10.1029/2007GL030295>, 2007
- 1610 Wohlfahrt, G., Hammerle, A., Haslwanger, A., Bahn, M., Tappeiner, U. and Cernusca, A.: Disentangling
1611 leaf area and environmental effects on the response of the Net Ecosystem Co2 Exchange to
1612 diffuse radiation, *Geophysical Research Letters*, 35(16). doi:10.1029/2008gl035090, 2008.
- 1613 Wohlfahrt, G., Hammerle, A., Niedrist, G., Scholz, K., Tomelleri, E. and Zhao, P.: On the energy balance
1614 closure and net radiation in complex terrain, *Agricultural and Forest Meteorology*, 226–227, pp.
1615 37–49. doi:10.1016/j.agrformet.2016.05.012, 2016.
- 1616 Yang, K., N. Guyennon, L. Ouyang, L. Tian, G. Tartari, and F. Salerno: Impact of summer monsoon on
1617 the elevation-dependence of meteorological variables in the south of Central Himalaya.
1618 *International Journal of Climatology*. 5293: 1748-1759. doi:10.1002/joc.5293, 2017.